

# MGGPOD: a Monte Carlo Suite for Modeling Instrumental Line and Continuum Backgrounds in Gamma-Ray Astronomy

G. Weidenspointner<sup>1,2,3</sup>, M.J. Harris<sup>1,2</sup>, S. Sturmer<sup>1</sup>, B.J. Teegarden

*NASA Goddard Space Flight Center, Code 611, Greenbelt, MD 20771, USA*

`Georg.Weidenspointner@cesr.fr`

and

C. Ferguson

*Physics Department, University of Southampton, Southampton, SO17 1BJ, UK*

## ABSTRACT

Intense and complex instrumental backgrounds, against which the much smaller signals from celestial sources have to be discerned, are a notorious problem for low and intermediate energy  $\gamma$ -ray astronomy ( $\sim 50$  keV – 10 MeV). Therefore a detailed qualitative and quantitative understanding of instrumental line and continuum backgrounds is crucial for most stages of  $\gamma$ -ray astronomy missions, ranging from the design and development of new instrumentation through performance prediction to data reduction. We have developed MGGPOD, a user-friendly suite of Monte Carlo codes built around the widely used GEANT (Version 3.21) package, to simulate *ab initio* the physical processes relevant for the production of instrumental backgrounds. These include the build-up and delayed decay of radioactive isotopes as well as the prompt de-excitation of excited nuclei, both of which give rise to a plethora of instrumental  $\gamma$ -ray background lines in addition to continuum backgrounds. The MGGPOD package and documentation are publicly available for download from <http://sigma-2.cesr.fr/spi/MGGPOD/>.

We demonstrate the capabilities of the MGGPOD suite by modeling high resolution  $\gamma$ -ray spectra recorded by the Transient Gamma-Ray Spectrometer (TGRS) on board *Wind* during 1995. The TGRS is a Ge spectrometer operating

---

<sup>1</sup>Universities Space Research Association, 7501 Forbes Blvd., Seabrook, MD 20706-2253, USA

<sup>2</sup>Centre d'Etude Spatiale des Rayonnements, 9 Avenue Colonel Roche, 31028 Toulouse Cedex 4, France

<sup>3</sup>ESA Fellow

in the 40 keV to 8 MeV range. Due to its fine energy resolution, these spectra reveal the complex instrumental background in formidable detail, particularly the many prompt and delayed  $\gamma$ -ray lines. We evaluate the successes and failures of the MGGPOD package in reproducing TGRS data, and provide identifications for the numerous instrumental lines.

*Subject headings:* instrumentation: miscellaneous, methods: numerical, methods: data analysis, line: identification

## 1. Introduction

Due to the opacity of the Earth’s atmosphere, astronomical observations in the  $\gamma$ -ray regime must be performed at the top of the atmosphere or in space, regions that are pervaded by intense radiation fields. Interactions of the particle radiations with the instrument and spacecraft materials result in a complex instrumental background. Discerning the much smaller signals from celestial sources against this strong background is the single worst problem for  $\gamma$ -ray astronomy at low and intermediate energies of about 50 keV – 10 MeV. Thus a detailed qualitative and quantitative understanding of the physical processes giving rise to instrumental line and continuum backgrounds is crucial for most stages of  $\gamma$ -ray astronomy missions, ranging from the design and development of new instrumentation through performance prediction and mission planning to data reduction.

Obtaining quantitative estimates of instrumental backgrounds is rendered very difficult by the complexity of the physics involved. The instrumental background of a given mission has a complicated dependence on its specific radiation environment, which in turn depends on the mission’s orbit and epoch of operation, and on the details of the instrument design (the detector material, the field-of-view, active and passive shielding, and the amount and distribution of active and passive material). For many years semi-empirical methods and scaling laws have been used to predict the instrumental background of a given instrument based on data from past missions and a well-developed understanding of the relevant physics (see e.g. Dean, Lei & Knight 1991; Gehrels 1992). However, the subtleties and complexities involved in scaling from one combination of radiation environment and instrument design to another degraded the accuracy of these predictions (Dean et al. 2003).

The advent of particle transport codes capable of dependably representing the fundamental physics involved, together with recent advances in computer processing speed, make *ab initio* Monte Carlo simulation a feasible approach for obtaining quantitative estimates of instrumental backgrounds (Dean et al. 2003). In this approach, model spectra of the mission

specific radiation environment and its time variability are combined with a computer representation of the geometrical structure and material composition of the  $\gamma$ -ray instrument and the rest of the spacecraft to track the trajectories and interactions of the incident particles and their secondaries, and to record their energy deposits throughout the system. One of the first Monte Carlo packages developed for this purpose was the University of Southampton's GGOD suite, which provided the capability of modeling instrumental line and continuum backgrounds due to the delayed decay of radioactive isotopes produced in particle interactions. GGOD has been applied to modeling numerous  $\gamma$ -ray instruments, among them the GRIS balloon spectrometer, TGRS on board *Wind*, BATSE on board the *Compton Gamma-Ray Observatory (CGRO)*, IBIS and SPI on board *INTEGRAL*, and BAT on board *Swift* (see Lei et al. 1996; Dean et al. 2003, and references therein). Monte Carlo codes with similar capabilities have been developed by other groups and were validated using e.g. data from the Oriented Scintillation Specrometer Experiment (OSSE) on board *CGRO* (Dyer et al. 1994) or from the Ge spectrometer on board the *HEAO-3* mission (Graham et al. 1997).

Motivated by the need for accurate modeling of the instrumental line and continuum background expected for the Ge spectrometer SPI on board the *INTEGRAL* mission, we have improved the GGOD suite and combined it with the user-friendly NASA/GSFC MGEANT package, which is e.g. used for SPI response simulations (Sturmer et al. 2000, 2003). Both the MGEANT and GGOD codes are based on the widely used GEANT Detector Description and Simulation Tool (Version 3.21, Brun et al. 1995). In order to include photons due to the prompt de-excitation of excited nuclei produced in neutron captures, inelastic neutron scattering, and spallations in our simulations, we created the PROMPT package, which is integrated into the MGEANT and GGOD codes. The resulting suite of Monte Carlo packages, named MGGPOD, supports *ab initio* Monte Carlo simulations of both prompt and delayed instrumental backgrounds, including the plethora of instrumental  $\gamma$ -ray lines. The MGGPOD suite and documentation are available to the public for download from <http://sigma-2.cesr.fr/spi/MGGPOD/>. The various MGGPOD packages, including GEANT Version3.21, have all been developed in the FORTRAN77 programming language and therefore *cannot* be used with the more recent Geant4 toolkit, which has been developed at CERN using the C++ language.

We demonstrate the capabilities of the MGGPOD suite by modeling high resolution  $\gamma$ -ray spectra recorded by the Transient Gamma-Ray Spectrometer (TGRS) on board *Wind* during 1995 (earlier modeling using the GGOD suite has been reported by Lei et al. 1996; Diallo et al. 2001). The TGRS is a Ge spectrometer operating in the 40 keV to 8 MeV range (Owens et al. 1995). Due to its fine energy resolution, these spectra reveal the complex instrumental background in formidable detail, particularly the many prompt and delayed  $\gamma$ -ray lines for which we provide identifications. We evaluate the successes and failures of the

MGGPOD package in reproducing the TGRS line and continuum backgrounds. A synopsis of the TGRS results presented here, and preliminary modeling results for the SPI spectrometer, can be found in Weidenspointner et al. (2004a). Recently, preliminary MGGPOD results have also been presented for the *Rewven Ramaty High-Energy Solar Spectroscopic Imager* (*RHESSI*, described in Smith et al. 2002) by Wunderer, Smith, & Weidenspointner (2004). A brief overview of the capabilities, functioning, and structure of the MGGPOD package has been given by Weidenspointner et al. (2004b).

In this paper, we provide an overview on a variety of aspects pertaining to the production and characterization of instrumental backgrounds in  $\gamma$ -ray astronomy in § 2. The capabilities, functioning, and structure of the MGGPOD package, including the modeled physics, are described in § 3. Our MGGPOD modeling of TGRS data, our TGRS instrumental line identifications, and detailed comparisons of data and simulation are given in § 4. A summary of our results and concluding remarks can be found in § 5.

## 2. Instrumental Background

In this section we provide an overview of a variety of aspects pertaining to the production and characterization of instrumental backgrounds in  $\gamma$ -ray astronomy. The instrumental background of a given  $\gamma$ -ray instrument has a complicated and complex dependence on its specific radiation environment and the details of the instrument design. The radiation environment, i.e. the ambient photon and particle radiation fields, their spectral and angular distributions, as well as their time histories, are a sensitive function of a mission’s orbit relative to the Earth and the geomagnetic field. The photons and particles that constitute the local radiation environment interact with detector and instrument and spacecraft structures through a wide variety of physical processes, producing secondary photons and particles, as well as radioactive nuclei, which, upon their (delayed) decay, give rise to further secondaries. These primary and secondary photons and particles can result in detector triggers that pass all logical and electronic criteria required for proper events due to photons from celestial sources; these triggers constitute the instrumental background. In a given radiation environment, the strength and spectrum of the instrumental background are strongly influenced by details of the instrument design such as the choice of detector material, the field-of-view, active and passive shielding, and the amount and distribution of active and passive material.

Among the radiation fields that are potential sources of instrumental background in  $\gamma$ -ray astronomy missions are cosmic rays (Galactic cosmic rays, solar energetic particles, and anomalous cosmic rays), geomagnetically trapped particles, Earth albedo radiations, diffuse cosmic X and  $\gamma$  radiation, and locally produced secondary radiation (see e.g. Stassinopoulos

1989; Klecker 1996; Dean et al. 2003, and references therein). An accurate description of the radiation environment clearly is of great importance for instrumental background estimates. Table 1 provides a summary (for quick reference) of some salient features of the radiation background components described below.

- *Galactic cosmic rays:* Galactic cosmic rays primarily consist of protons (about 85% by number), followed by  $\alpha$  particles ( $\sim 12\%$ ), and electrons ( $\sim 2\%$ ); the remainder are heavier nuclei. For kinetic energies above about 10 GeV/nucleon solar modulation is no longer effective and the differential energy spectrum of cosmic rays can be approximated by an  $E^{-2.7}$  power law. This particle radiation is a dominant source of instrumental background for missions that spend most of their time outside the Earth’s magnetosphere or at least above the radiation belts, but may be less significant for balloon borne experiments or missions in low-Earth orbits (LEOs) because the geomagnetic field acts as a momentum/energy filter requiring that a charged particle must exceed a minimum rigidity<sup>1</sup> (the so-called cut-off rigidity) to reach a given location within the magnetosphere. For LEOs the incident cosmic radiation therefore varies with time because the local cut-off rigidity changes as the spacecraft follows its trajectory. Outside the magnetosphere the only source of temporal variation in the incident cosmic radiation is solar modulation, which affects particles with kinetic energies less than a few GeV/nucleon. At balloon altitudes and in LEO the geomagnetic cutoff and Earth shadowing result in a highly anisotropic cosmic-ray intensity; outside the magnetosphere cosmic rays can be assumed isotropic.
- *Solar energetic particles and anomalous cosmic rays:* Solar energetic particles (SEPs) are produced in violent energy releases on the Sun such as flares or coronal mass ejections (CMEs). They are reinforced on their way to Earth by interplanetary particles accelerated by the shock waves from CMEs. During these times their flux can be enormously high compared to other particle radiations. SEPs have energies up to several hundred MeV/nucleon and hence a lower rigidity than Galactic cosmic rays. Missions in LEOs and balloon experiments are therefore shielded from most of them, while SEPs can be a dominant temporary source (up to a few days) of instrumental background for missions outside the magnetosphere. Like SEPs, anomalous cosmic rays are mainly a concern for missions outside the magnetosphere; because they consist mostly of heavy nuclei they can be effective producers of secondaries in nuclear interactions. The inten-

---

<sup>1</sup>The rigidity  $R$  of a particle of charge  $q$  and momentum  $p$  is given by:  $R = \frac{pc}{q}$ . A cut-off rigidity of 10 GV, which is a “typical” value for LEOs with low inclination, implies that a cosmic-ray proton must exceed a kinetic energy of about 9.1 GeV to reach the spacecraft

sity of anomalous cosmic rays is much more strongly effected by the solar cycle than that of Galactic cosmic rays.

- *Geomagnetically trapped radiation:* Out to a few Earth radii, the geomagnetic field can be well approximated by a dipole. Charged particles can be magnetically trapped in such a dipole field and stored in so-called radiation belts in the geomagnetic equatorial plane. The most abundant trapped particle species are protons and electrons. Protons, which are of main concern for instrumental backgrounds, are trapped in a single belt, with the maximum proton intensity occurring at an altitude of  $\lesssim 1$  Earth radius. The energies of the protons extend up to several hundred MeV; their angular distribution can be highly anisotropic (Whatts, Parnell, & Heckman 1989). The geomagnetic dipole is offset from the Earth’s center, therefore the proton belt appears to extend to lower altitudes over the coast of Brazil – this area is usually referred to as the South Atlantic Anomaly (SAA). Because of its intensity this trapped proton radiation is avoided as much as possible by  $\gamma$ -ray missions. However, the SAA usually can not be avoided altogether for missions in LEOs. If encountered, passages through the SAA are a dominant source for the production of radionuclides in the instrument and spacecraft materials (Kurfess et al. 1989; Weidenspointner et al. 2001). The SAA dosage received by a mission in LEO strongly depends on the orbit’s altitude and inclination.
- *Earth albedo radiation:* When entering the Earth’s atmosphere Galactic cosmic-ray particles interact violently with the air nuclei, initiating nuclear interaction cascades that ultimately result in the production of a multitude of secondaries of relatively low energy. The most important of these secondaries for  $\gamma$ -ray experiments at balloon altitudes and in LEO are photons and neutrons. At balloon altitudes, the angular distribution of these secondaries is highly anisotropic, and their intensity depends on the local geomagnetic cut-off rigidity and on the depth in the atmosphere (see e.g. Gehrels 1985, and references therein). Depending on energy, both albedo photons and neutrons can constitute strong and anisotropic radiation fields for missions in LEO, and are dominant background sources for balloon experiments. The relative importance of the Earth’s  $\gamma$ -ray albedo as a diffuse photon source increases with energy, above about 35 MeV it is 10–100 times more intense than the diffuse cosmic  $\gamma$  radiation (Thompson & Simpson 1981). The energy distribution of albedo neutrons extends from thermal energies to at least several hundred MeV. The intensity of albedo  $\gamma$ -rays (Thompson & Simpson 1981; Harris, Share, & Leising 2003) and neutrons (Weidenspointner et al. 1996; Morris et al. 1998) varies with the local geomagnetic rigidity and with the solar cycle.
- *Diffuse cosmic X and  $\gamma$  radiation:* The diffuse cosmic X and  $\gamma$  radiation is of great

astrophysical interest in its own right (e.g. Weidenspointner & Varendorff 2001); however, it constitutes a background against which all other observations must be made. For the purpose of background simulations, the diffuse cosmic X and  $\gamma$  radiation can be considered isotropic (Kinzer et al. 1997; Sreekumar et al. 1998; Weidenspointner et al. 2000), and its energy spectrum constant in time and unaffected by the geomagnetic field. For missions in LEO the shielding effect of the Earth needs to be taken into account. In addition, at balloon altitudes there is direction-dependent attenuation by the atmosphere, although the atmospheric  $\gamma$  radiation usually dominates.

- *Internally produced secondary particles:* The photons and particles of the external radiation fields described above interact with the instrument and spacecraft structures through a wide variety of physical processes (see below), producing a multitude of secondary particles such as photons, electrons and positrons, neutrons, protons and heavier nuclei. Because this locally produced secondary radiation is produced by the external radiation fields it is therefore not a component of the radiation environment in the same sense as the external components. We list here the secondary radiation as a separate component of the radiation environment because it is treated as such in semi-empirical calculations of instrumental backgrounds (e.g. Gehrels 1992). In *ab initio* Monte Carlo calculations, the topic of this paper, these secondary particles are derived from the modeling of the interactions of the external radiation fields, which are the only input.

The photons and particles of the radiation environment interact through a wide variety of processes with the instrument and spacecraft structures and contribute to the instrumental background in different ways. Backgrounds due to external photon fields are most important for instruments with poor spatial resolution and a large field-of-view. The photons trigger the detector either by entering through the field-of-view (aperture flux) or by entering through the veto shield without it being triggered (shield leakage). Energetic protons (and heavier nuclei) are a major source of instrumental background. They may pass through the instrument and spacecraft suffering only slight energy losses due to ionization in the traversed materials. However, they may also undergo a catastrophic nuclear interaction with a single nucleus, creating a potentially large number of secondary particles such as pions, nucleons, and light nuclei; usually a relatively heavy product nucleus is left behind. The secondary particles may be energetic enough to initiate further nuclear interactions with other nuclei, their decay (e.g. pions) can result in the generation of secondary photons, electrons, and positrons, and the de-excitation of residual nuclei gives rise to more secondary particles (mainly photons).

All of these processes and interactions occur on timescales that are short compared to

typical timescales for event processing by the instrument electronics (which typically are a few to about 100  $\mu\text{s}$ ) and contribute to the so-called *prompt* instrumental background. Depending on energy, veto shields can reduce prompt background components by a few orders of magnitude. Some of the product nuclei resulting from interactions of protons or other hadrons may not be stable and emit further secondary particles when undergoing radioactive decay. Depending on the lifetime of the unstable product nucleus, the time delay between its production and its decay may be much longer than typical instrumental event processing timescales, contributing to the so-called *delayed* instrumental background. For satellite missions the long-term build-up of delayed background due to long-lived isotopes (e.g.  $^{22}\text{Na}$ ,  $T_{1/2} = 2.7$  y) is very clearly visible (Kurfess et al. 1989; Weidenspointner et al. 2001). The best strategy to minimize delayed instrumental background is to minimize the amount of passive material in the instrument, particularly in the vicinity of the detectors. More positively, the time-scale of the long-term build-up is characteristic of the nuclear half-life, and a valuable key to identification of the nucleus involved.

Neutrons are another major source of both prompt and delayed instrumental background components. Unlike protons, neutrons can traverse veto shielding without triggering it and produce prompt background *within* the detector through elastic and inelastic scattering (by passing energy to the recoil nucleus and de-excitation) as well as neutron capture (de-excitation of the product nucleus). Outside the veto shield the de-excitation of product nuclei from neutron induced nuclear interactions, including neutron capture, also contribute to the prompt background. Some of these product nuclei are unstable, and their radioactive decay adds to the delayed background.

An important aspect of the instrumental background is the presence of many lines. The position, strength, and shape of instrumental lines are relevant because they can interfere with spectroscopy of astrophysical  $\gamma$ -ray lines. Instrumental lines can result from prompt processes such as de-excitation of excited nuclei as well as from delayed radioactive decays. Instrumental lines can also be used as powerful diagnostics of the overall instrumental background, including continuum components. For example,  $\gamma$ -ray lines produced by isomeric transitions in Ge detectors can be used to estimate the neutron flux inside the veto shield, which then in turn allows an estimate of continuum backgrounds due to elastic and inelastic neutron scattering and neutron induced  $\beta$ -decays (e.g. Naya et al. 1996).

### 3. The MGGPOD Monte Carlo Simulation Suite

The MGGPOD suite is a user-friendly Monte Carlo simulation package that is applicable to all stages of space-based  $\gamma$ -ray astronomy missions. In particular, the MGGPOD suite

allows *ab initio* simulations of instrumental backgrounds – including the many  $\gamma$ -ray lines – arising from interactions of the various radiation fields within the instrument and spacecraft materials. It is possible to simulate both prompt instrumental backgrounds, such as energy losses of cosmic-ray particles and their secondaries, as well as delayed instrumental backgrounds, which are due to the decay of radioactive isotopes produced in nuclear interactions. MGGPOD can also be used to study the response of  $\gamma$ -ray instruments to astrophysical and calibration sources. The MGGPOD suite is therefore an ideal Monte Carlo tool for supporting most stages of  $\gamma$ -ray missions, ranging from instrument design to data reduction. Software and documentation are available to the public for download at the Centre d’Etude Spatiale des Rayonnements<sup>2</sup>. In this publication we focus on the physics simulated by the MGGPOD suite. Detailed practical advice for users on how to install and use this Monte Carlo package, including examples, can be found in the documentation available on the MGGPOD web site (see also Weidenspointner et al. 2004b).

MGGPOD is a suite of five closely integrated Monte Carlo packages, namely **MGEANT**, **GALOR**, **PROMPT**, **ORIHET**, and **DECAY**, each of which will be described in more detail below. The MGGPOD package resulted from a combination of the NASA/GSFC MGEANT (Sturmer et al. 2000, 2003) and the University of Southampton’s GGOD (Lei et al. 1996; Dean et al. 2003) Monte Carlo codes. Both were improved, and supplemented by the newly developed PROMPT package. The overall structure of the MGGPOD package is illustrated in Fig. 1. Depending on the simulated radiation field or  $\gamma$ -ray source distribution one or three steps, requiring two or three input files, are needed to obtain the resulting energy deposits in the detector system under study, as summarized in Table 2. In general, it is advisable to simulate each component of the radiation environment separately. MGGPOD distinguishes two classes of radiation fields. Class I comprises radiation fields for which only prompt energy deposits are of interest, such as celestial or laboratory  $\gamma$ -ray sources or cosmic-ray electrons. Class II comprises radiation fields for which additional delayed energy deposits resulting from the activation of radioactive isotopes need to be considered. Examples of Class II fields are cosmic-ray protons, or geomagnetically trapped protons.

For both of these classes, the simulation of the prompt energy deposits requires two input files: a mass model, and a model of the simulated radiation field. The mass model is a detailed computer description of the experimental set-up under study. It specifies the geometrical structure of instrument and spacecraft, the atomic and/or isotopic composition of materials, and sets parameters that influence the transport of particles in different materials. Each component of the radiation environment (and analogously for  $\gamma$ -ray sources) to which the

---

<sup>2</sup><http://sigma-2.cesr.fr/spi/MGGPOD/>

instrument is exposed is characterized by three quantities: the type of the incident particles, and their spectral and angular distributions. The prompt energy deposits are written to an output event file. In case of a Class II radiation field there is an additional output file which lists, for all nuclei produced in hadronic interactions, the product nucleus' identity along with the geometrical mass model element in which it was produced. From this file isotope production rates can be computed.

To simulate delayed energy deposits (Class II radiation field) two additional steps need to be taken. These require as input the time history of the radiation field which is responsible for the activation, and the previously calculated isotope production rates. Based on this information first the activity of each isotope produced in each structural element of the mass model is determined by ORIHET. Then, employing the MGEANT, GCALOR, and DECAY packages, these activities are used to simulate the delayed energy deposits due to radioactive decays in the instrument.

Combining prompt and delayed energy deposits from each component of the radiation environment and  $\gamma$ -ray sources, it is possible to obtain the total energy deposited in the system as a function of position and time. In the following, each of the five packages that constitute the MGGPOD simulation suite is described.

### 3.1. MGEANT

MGEANT is a multi-purpose simulation package developed by the Low Energy Gamma Ray Group (LEGR) at NASA/GSFC (Sturmer et al. 2000, 2003). It is based on the GEANT Detector Description and Simulation Tool (Version 3.21) created and supported by the Application Software Group, Computing Networks Division, at CERN Geneva, Switzerland (Brun et al. 1995). GEANT3 is designed to simulate the passage of elementary particles through an experimental set-up, which may be of considerable complexity. Although originally designed for high-energy physics experiments, GEANT3 has found applications in many other areas, including space science and specifically  $\gamma$ -ray astronomy. Within the MGGPOD suite, MGEANT (i.e. GEANT3) stores and transports all particles, and treats electromagnetic interactions from about 10 keV to a few TeV. In addition, MGEANT provides the option to use the GEANT Low-Energy Compton Scattering package GLECS, which provides more detailed physical models of the coherent (Rayleigh) and incoherent (Compton) photon scattering processes than those included in the standard GEANT3 distribution by taking into

account the kinetic energy of the bound electrons (Kippen 2002, 2004)<sup>3</sup>.

MGEANT was created to increase the versatility and user-friendliness of the GEANT3 simulation tool<sup>4</sup>. A modular, “object oriented” approach was pursued, giving MGEANT two main advantages over standard GEANT3. First, the instrument specific geometries and materials are provided via input files, rather than being hard-coded. Second, several event-generation beam models and spectral models are available (e.g. Sturmer et al. 2000, 2003). Beam models include a plane wave, an isotropic radiation field, astrophysical and calibration point sources, or a user defined sky map; spectral models include power law and exponential spectra, line emission, or user defined spectra. Furthermore, MGEANT can interactively display (using CERN’s PAW++ package) the geometric set-up as well as the particle trajectories – a very convenient capability when creating a mass model or defining and verifying beam parameters. In MGGPOD the only supported output file format is FITS, for which two different event list formats are available: 1) standard format where the total energy deposit in each detector (and in the anti-coincidence system) for each event is listed, and 2) extended format where the energy deposits and location of each interaction, the time of interaction, and the type of the interacting particle are also listed. The extended format was introduced to facilitate detailed instrument response studies, such as the pulse-shape discrimination (PSD) system of the *INTEGRAL* spectrometer SPI, or event reconstruction algorithms for advanced Compton telescope concepts.

MGEANT is therefore very well suited for rapid prototyping of detector systems, it can readily generate most of the radiation fields relevant to  $\gamma$ -ray astronomy, and it is set up to support detailed instrument response studies. The MGEANT simulation package and a user manual are available at the NASA/GSFC web site of the LEGR group<sup>5</sup>.

### 3.2. GCALOR

GCALOR (Zeitnitz & Gabriel 1994, 1999) is an interface between the CALOR89 package by (Gabriel et al. 1995) and the GEANT3 simulation tool. The CALOR89 package, designed to simulate calorimeter systems for high-energy physics detectors, simulates hadronic interac-

---

<sup>3</sup>Version 1.1 of MGGPOD, which is currently under development, will in addition provide the option to use the GLEPS package to take into account the polarization of the initial photon in Compton and Rayleigh scatterings (Kippen 2002).

<sup>4</sup>MGEANT does not work with the newly developed, C++ based, Geant4 toolkit.

<sup>5</sup><http://lheawww.gsfc.nasa.gov/docs/gamcosray/legr/mgeant/mgeant.html>

tions down to 1 MeV for nucleons and charged pions and down to thermal energies ( $10^{-5}$  eV) for neutrons. GCALOR incorporates the capability to perform hadronic interaction calculations in the GEANT3 framework by extracting the HETC (High Energy Transport Code) collision and evaporation model and the FLUKA model (which is already available in recent versions of GEANT3) from CALOR89. The HETC Monte Carlo code consists of two parts: the Nucleon Meson Transport Code (NMTC) and the Scaling Model (which provides a smooth transition between the NMTC and FLUKA regimes). For low energy neutrons the MICAP (Monte Carlo Ionization Chamber Analysis Package) neutron code by Johnson & Gabriel (1988) has been included into GCALOR, rather than the MORSE neutron transport code utilized in CALOR89<sup>6</sup>. The particle types and energy ranges covered by the four modules of GCALOR are:

- **NMTC**: nucleons 1 MeV to 3.5 GeV, charged pions 1 MeV to 2.5 GeV
- **Scaling Model**: nucleons and charged pions 3 GeV to 10 GeV
- **FLUKA**: nucleons and charged pions above 10 GeV, and for all energies for particle types not implemented in CALOR
- **MICAP**: neutrons  $10^{-5}$  eV to 20 MeV

Hadronic interactions between particles that are both heavier than individual nucleons, such as deuterium or helium nuclei, cannot be simulated with GCALOR. However, continuous energy losses, for example due to ionization of the matter traversed, are taken into account for all charged particles. The GCALOR package is publicly available at the Universität Mainz<sup>7</sup>.

When combining GCALOR with GEANT3 (or MGEANT), all particles are stored and transported by GEANT3. Electromagnetic interactions are simulated by GEANT3, hadronic

---

<sup>6</sup>The performance of MORSE is very similar to that of MICAP (Johnson & Gabriel 1987). However, MICAP is easier to interface with GEANT3 than MORSE (Zeitnitz & Gabriel 1994, Zeitnitz 2004, priv. comm.). The MORSE program uses an energy binning for neutron cross-sections and secondary energy distributions. Neutrons are generated only with these discrete energies. MORSE does account for particle multiplicities by assigning a weight to the generated secondaries. In contrast, MICAP uses pre-processed ENDF/B cross-section data and the number of energy points is not fixed, but depends on the isotope and the availability of cross-section data for this isotope. MICAP statistical weights for secondary particles are substantially smaller than those of MORSE, hence it is easier to generate discrete numbers of actually produced secondary particles which are then handed to GEANT3, which cannot treat statistical weights, for further processing.

<sup>7</sup><http://wswww.physik.uni-mainz.de/zeitnitz/gcalor/gcalor.html>

interactions are simulated by GCALOR. The GEANT3 plus GCALOR package therefore extends the capabilities of the standard GEANT3 tool to include hadronic interactions of charged particles down to 1 MeV and of neutrons down to thermal energies. Equally important, this package provides access to the energy deposits from all interactions as well as to isotope production anywhere in the geometrical set-up.

Originally, GCALOR/MICAP utilized only ENDF/B (Evaluated Nuclear Data Files version B) neutron data. Unfortunately, these data, available e.g. at the National Nuclear Data Center (NNDC) at Brookhaven National Laboratory<sup>8</sup>, do not cover all elements or isotopes. In particular, individual neutron cross-sections for the five natural Ge isotopes are missing. These cross-sections, which are clearly of great importance for simulations of instrumental backgrounds in Ge spectrometers, were generated based on JENDL (Japanese Evaluated Nuclear Data Library<sup>9</sup>) data by Zeitnitz (2001, priv. comm.).

Some of the low-mass residual nuclei produced in spallations as modelled by GCALOR are very neutron rich, particularly if the incident projectile is energetic (e.g. a primary cosmic-ray proton). Most of these neutron-rich nuclei result from a failure of the intranuclear cascade/evaporation model used in GCALOR (Gabriel 2004, priv. comm.). Some neutron rich nuclei have been identified in nuclear experiments and found to have short lifetimes of less than 1 s. Neutron rich nuclei are unstable against the emission of one or several neutrons, a process that affects the number and energy distribution of secondary neutrons. To include this source of secondary neutrons into our simulations, MGGPOD checks whether light product nuclei ( $Z \leq 8$ ) are unstable against neutron emission, exploiting existing data whenever available (Firestone 1996), and mandates neutron emission if appropriate, converting the unstable original product nucleus into the highest-mass isotope that has no neutron exit channel.

### 3.3. PROMPT

The PROMPT package was created for simulating the prompt de-excitation of excited nuclei produced by neutron capture, inelastic neutron scattering, and spallation<sup>10</sup>. The

---

<sup>8</sup><http://www.nndc.bnl.gov/>

<sup>9</sup><http://wwwndc.tokai.jaeri.go.jp/jendl/jendl.html>

<sup>10</sup>Although spallation is physically defined in terms of the evaporation model (see § 3.3.2), for the purpose of MGGPOD it is defined to comprise all hadronic interactions other than neutron capture which result in a product nucleus that is different from the target nucleus. We will, however, assume the validity of the evaporation model for all such interactions in our treatment

PROMPT package consists of a data base containing information on the de-excitation of a large number of nuclei, and of code to access these data and to generate random samples of de-excitation particles (photons and electrons). When simulating prompt hadron-induced backgrounds with MGGPOD, the MGEANT, GCALOR, and PROMPT packages are linked into a single executable (see Fig. 1). Each time a secondary nucleus is produced in a nuclear interaction as simulated by GCALOR, PROMPT is called to model the de-excitation cascade. In GCALOR, prompt photons are generated for a few hadronic interactions, however, in general these photons are “statistical” and continuous – they do not reflect the actual discrete nuclear levels and the well-known selection rules for transitions between them. This approximate treatment proved sufficient for modeling calorimeters for high-energy physics detectors (Zeitnitz & Gabriel 1994), but is clearly insufficient for detailed modeling of instrumental  $\gamma$ -ray backgrounds. Therefore any prompt photons generated by GCALOR are replaced with those returned by the PROMPT package. With the exception of a few selected neutron rich nuclei (see previous §), PROMPT treats all secondary nuclei as stable, irrespective of their lifetime; all radioactive decays are treated in a subsequent simulation step using the DECAY package (see Fig. 1 and Table 2). A de-excitation cascade may proceed through one or more isomeric levels; if so, their effect on the time sequence of de-excitation particle emission is taken into account approximately, as described in §3.5.

We developed the PROMPT package in the spirit of the compound nucleus model, in which it is assumed that the reaction process can be separated into independent incoming and outgoing channels with a well-defined intermediate compound state. We rely on the GCALOR package for a complete specification of the incoming channel in the three classes of prompt reaction, i.e. neutron capture, inelastic neutron scattering, and spallation. Beyond a determination of the daughter nucleus, the outgoing channel is, however, at best incompletely specified by GCALOR; in particular, de-excitation photons are either missing or incorrect, as described above. In other words, GCALOR generates a known daughter nucleus in an unknown excited state with unknown de-excitation properties. In addition, the distribution of excited states left behind by the three types of prompt reaction is not generally known – unlike the case of radioactive decay, where the excited state in the daughter has a well-known probability from extensive measurements of branching ratios (see § 3.5). To create the PROMPT package we therefore had to derive (simple) recipes for selecting an excited state in the daughter nucleus and then modeling its de-excitation into known lower energy levels. Our approach is to use a probabilistic recipe to specify the intermediate excited state of the compound daughter nucleus, and a further *ansatz* to specify the de-excitation of the excited state into known lower levels. When generating de-excitation particles (usually photons), we do not take into account Doppler broadening due to the motion of the nucleus during de-excitation, which is relevant for short-lived levels with  $T_{1/2} \lesssim 0.5$  ps (Evans et al. 2002).

### 3.3.1. Neutron Capture and Inelastic Neutron Scattering

In the case of neutron capture and inelastic neutron scattering, the excitation energies involved are fairly low, and the processes involved are fairly well understood. We selected the excited state of the compound nucleus at random from a level density formula, by which the probability of obtaining an energy level depends on its spin  $J$ , parity  $\pi$  and excitation energy  $U$ . The value of  $U$  was obtained from GCALOR from the kinematics of the incoming channel reaction. The distribution of spins and parities follows the angular part of the Bethe level density formula as parametrized by Mughabghab & Dunford (1998); this angular part contains a weak dependence on  $U$  which we neglected (the overall density contains an exponential in  $\sqrt{U}$ , but we are only interested in the relative probabilities of different  $J$  and  $\pi$  values). Having selected an excited state in this way, we assumed that it coupled to known states of lower excitation energy (from the ENSDF database<sup>11</sup>) by an electric dipole (E1) transition – the spins and parities of the lower states were required to obey the well-known E1 selection rules for coupling to  $J^\pi$ , and if none were permitted we assumed magnetic dipole (M1) transitions. The probability of a transition from an excited state to a permitted level  $x$  was assumed to be proportional to  $(U - U_x)^3$ , which holds approximately for dipole transitions (Blatt & Weisskopf 1952). The specific prescriptions for generating prompt photons for these two neutron-induced reactions are outlined in the following, and illustrated in schematic form in Figs. 2 and 3.

For neutron captures on nuclei with  $A > 3$  (M)GEANT and GCALOR specify the kinetic energy of the incident neutron, the target and the product nucleus, and the recoil energy  $E_r$  of the product nucleus. We estimated the excitation energy  $U$  of the product nucleus as the sum of its neutron separation energy  $S_n$  (taken from Firestone 1996, typically several MeV), which is the excitation energy after capturing a thermal neutron, and the kinetic energy of the incident neutron  $E_k$ ; the recoil energy of the product nucleus typically is only a few eV and therefore negligible. We obtain the probability of a compound nucleus level having given values of  $J^\pi$  from the Mughabghab & Dunford (1998) level density formula as described above; however, we make the approximation that it is always evaluated at excitation energy  $U = S_n$ , which is justified by the weak variation of the  $J^\pi$  distribution on  $U$ . The de-excitation cascade which follows was treated by two different *ansätze*, depending on the value of  $J^\pi$ ; those values which are compatible with thermal neutron capture were simply assigned the branching ratios from the extensive thermal neutron database maintained by NNDC, while all other  $J^\pi$  values were assumed to de-excite by the E1 mechanism described above. Thermal neutrons couple to the target nucleus by low partial waves in the incoming channel

---

<sup>11</sup>Evaluated Nuclear Structure Data Files (ENSDF) are available at the NNDC (see footnote 11).

(we assumed s-wave), so that the corresponding  $J^\pi$  in the compound nucleus are easily specified, given the target nucleus' ground state. For example, in the common case of an even-even target ( $0^+$ ), an s-wave corresponds to  $\frac{1}{2}^+$  in the compound nucleus. Our motivation was to exploit the very large amount of thermal neutron experimental data available in this special case. The product nuclei for which the prompt de-excitation cascade after neutron capture is modeled in these ways are listed in Table 3.

For inelastic neutron scattering on nuclei with  $A > 4$  (M)GEANT and GCALOR specify, among other quantities, the kinetic energy of the incident neutron  $E_k$ , the recoil nucleus and its kinetic energy  $E_r$ , as well as that of the scattered neutron  $E'_k$ . The excitation energy of the recoil nucleus  $U$  is assumed to be  $U = E_k - E'_k - E_r$ . In general, the GCALOR cross-sections are accurate enough to reflect the lowest levels. However, above about 1–2 MeV the derived excitation energies approach a “continuum”. Modeling of the de-excitation cascade depends on the excitation energy  $U$ . If it is less than or equal the energy of the highest known level with transition data in ENSDF,  $E_h$ , then the initial level of the de-excitation cascade is chosen to be the level with transition data whose energy is closest to  $U$ . If  $U$  is greater than  $E_h$  then we assume a single initial transition from  $U$  down to any of those known levels for which spin-parity and transition probability data exist. The probability for this initial transition is calculated from the standard spin-parity distribution and the dipole selection rules as indicated above. The spin-parity distribution is evaluated at a reference energy  $E_{ref}$  chosen for each nucleus to be approximately where the inelastic neutron scattering cross-section peaks according to JENDL, which characteristically is around 10 MeV. As in the case of neutron capture (where we used  $U = S_n$ ), we assume that the calculated probability distribution for the initial transition from  $E_{ref}$  applies to all excitation energies  $U$  greater than  $E_h$ . This is justified by the weak dependence of this distribution on  $U$ . In the de-excitation cascade from this level at excitation energy  $U$  the energy of the initial transition is increased by  $U - E_{ref}$ . The recoil nuclei for which the prompt de-excitation cascade after inelastic neutron scattering is modeled are listed in Table 3.

The existence of asymmetrically broadened triangular or “sawtooth” shaped features extending in energy above the lines from the lowest energy neutron inelastic scatters has been recognized by several authors in both laboratory (Bunting & Kraushaar 1974) and flight (Wheaton et al. 1989; Evans et al. 2002; Weidenspointner et al. 2003) data, and are seen in our data also. They arise from the summed energy depositions by the recoiling Ge nucleus and by the de-excitation photon(s). These features are automatically predicted by (M)GEANT and GCALOR and furnish a comparison between the simulation and the behavior of the spectrometer.

### 3.3.2. Spallation

For spallation reactions (M)GEANT and GICALOR specify the type and kinetic energy and momentum of the incident particle, the target nucleus, and the types, energies and momenta of all reaction products. However, because GICALOR conserves energy and momentum for any interaction only on average, but not rigorously for an individual case, it is not possible to obtain a meaningful estimate of the excitation energy  $U$  of any reaction product from kinematics. Nor are experimental cross-sections available for production of such individual levels, which are extremely numerous. However, some general rules about the distribution of  $U$  values follow from the evaporation model, which is the generalization of the compound nucleus model to particle emission (Weisskopf & Ewing 1940). Proton-induced spallation reactions at high energy leave the compound nucleus in a very broad distribution of excitation energies, which can be thought of as a thermal distribution  $\sim \exp(-U/kT)$  for some temperature parameter  $T$  (unlike heavy-ion collisions, which tend to select collective states such as the high-spin yrast levels: Galin 2001). If  $T$  exceeds the nucleon separation energy one or more nucleons are likely to be emitted (neutrons above  $S_n$  being favored, since there is no Coulomb barrier). The generation of a daughter nucleus by GICALOR implies that neutron emission has ceased, which in turn implies that  $T < S_n$ . Characteristic values of  $S_n$  are several MeV; the fact that the thermal distribution has a substantial “tail” at energies above  $T$  implies that neutron emission only ceases when  $T$  falls far enough below  $S_n$  for the “tail” to become negligible. Experiments attempting to achieve high  $T$  in residual nuclei left behind by proton reactions on nuclei between Ag and Au have attained up to  $T \simeq 5$  MeV, with values 3–4 MeV being characteristic (Ledoux et al. 1998). On this basis we assumed that the known excited states  $U_x$  in spallation product nuclei were distributed according to the formula  $(2J_x + 1) \exp(-U_x/3 \text{ MeV})$ . A sketch of the procedure followed once particle emission has stopped is given in Fig. 4.

A key assumption behind this type of argument is that nuclear energy levels can be treated statistically, which is recognised to become less and less valid as the nuclear mass  $A$  falls below about 30 (Holmes et al. 1976). We found that, in practice, this thermal approximation cannot be used at all for  $A < 20$  since far too many lines are predicted in the simulation. On the other hand, the relatively small number of individual levels involved means that data on experimental cross-sections to individual levels of  $A < 20$  nuclei are in some cases quite complete. Ramaty, Kozlovsky, & Lingenfelter (1979) reviewed these cases, and we have obtained from their compilation the distribution of excited states for the nuclei in Table 4 when these are produced by spallation. The de-excitation of all other nuclei with  $A < 20$  was omitted from the simulation.

The statistical model is also expected to break down for low incident particle energies

(below a few MeV). In particular, this applies to spallations that are induced by secondary neutrons and protons. In these cases individual levels, rather than a statistical distribution parameterized by  $T$ , will be excited. In addition, the difference in level distributions produced by protons and neutrons (which we have otherwise ignored) will be important.

### 3.4. ORIHET

The original ORIHET program was developed for the GGOD Monte Carlo suite (Lei et al. 1996; Dean et al. 2003). It is an adaptation of the Oak Ridge Isotope Generation and Depletion code ORIGEN, which was designed to calculate the build-up and decay of activity in any system for which the nuclide production rates are known. To do so, ORIHET has a built-in data base containing the half-lives and decay channels of a large number of radio-isotopes. Currently, ORIHET returns the activity at a given time for two different radiation histories: constant irradiation, and “cooling down” after constant irradiation. In the first case, it is assumed that nuclei are produced at a constant rate for a given time period. This model is useful for simulating instrumental backgrounds for missions in radiation environments that are relatively stable, or for deriving average instrumental backgrounds for missions exposed to variable radiation fields as are encountered e.g. in LEOs. In the second case, it is assumed that nuclei are produced at a constant rate for a given period of time during which production and decay compete, then the production ends and the radio-isotopes decay for a given “cool-down” period. This model is e.g. useful for estimating the instrumental background due to transits through the SAA.

The original ORIHET radionuclide data base did not include all isotopes relevant for simulations of instrumental backgrounds in  $\gamma$ -ray experiments. Specifically, for some isotopes which can be produced in their ground state as well as an isomeric state, such as  $^{24}\text{Na}$ , the isomeric state was absent from the original data base. For MGGPOD, we have changed ORIHET to include all isomers missing in the original data base which produce significant  $\gamma$ -ray lines identified in spectra of TGRS or other Ge spectrometers. In addition, we corrected the treatment of  $\alpha$ -decays, which in the original data base were treated as  $\beta$ -decays.

### 3.5. DECAY

As was ORIHET, the original DECAY package was created for the GGOD suite (Lei et al. 1996; Dean et al. 2003). The DECAY package is the analog of PROMPT for simulating radioactive decays. It consists of a data base containing information on the decays of a large

number of radioactive isotopes, and of code to access these data and to generate random samples of decay particles. Linking the MGEANT, GCALOR, and DECAY packages into a single executable (see Fig. 1 and Table 2) enables one to simulate the decays of a given radio-isotope with a given activity over a given time period at any location in the geometric set-up.

To generate the DECAY data base, information concerning the decay schemes, such as branching ratios for  $\beta^-$ ,  $\beta^+$  and electron capture (EC) decays, internal transition (IT), and  $\alpha$ -decay channels, as well as the energy levels and  $\gamma$ -ray to internal conversion electron branching ratios, was taken from ENSDF. These data have been supplemented with information on X-ray and Auger electron fluorescence yields and energies as given in Firestone (1996).

In developing MGGPOD, we improved and expanded the DECAY package. The number of isotopes in the data base was increased, and data base and code upgraded to simulate approximatively isomeric levels (these sometimes give rise to significant instrumental lines in  $\gamma$ -ray detectors) as described below. Information on the emission of internal conversion electrons is very incomplete in ENSDF data. For a few isotopes relevant for Ge detectors we corrected the data files (e.g. for the 691 keV E0 transition in  $^{72}\text{Ge}$ , for which photon emission is not possible).

The de-excitation cascade of a daughter nucleus may proceed through one or more isomeric levels, which can have a significant effect on the time sequence of the emission of de-excitation particles. DECAY has the capability to account for isomeric levels in a de-excitation cascade in an approximate way by simulating the de-excitation particles in batches or groups; PROMPT applies the same approach to prompt de-excitations. In the simulations, a detector time resolution,  $\tau$ , can be defined (which approximates the shaping time of the detector electronics). Levels for which no lifetime information is available are assumed to have negligible lifetime and hence to decay instantaneously. For a level with finite lifetime, each time a cascade is simulated a decay time,  $t$ , is randomly calculated based on the lifetime, i.e. it is assumed that once the de-excitation cascade reaches this level the cascade does not proceed until a time  $t$  has passed. The simple algorithm to group the decay particles is as follows. If no level with finite lifetime is involved, all de-excitation particles are assumed to be emitted instantaneously. If one level with finite lifetime is involved, in case  $t \geq \tau$  the particles are assumed to be emitted in two batches (all particles emitted in the transitions from the initial level to the isomeric level, and all particles emitted in the subsequent transitions from the isomeric level to the ground state of the daughter nucleus); otherwise ( $t < \tau$ ) all particles are assumed to be emitted within  $\tau$  and hence are started simultaneously in the simulation. If two or more levels with finite lifetime are involved, the

procedure is slightly more complicated and becomes iterative. Let us assume there are  $n$  such levels, with randomly selected decay times  $t_i, i = 1, \dots, n$ . If  $t_1 \geq \tau$ , then all particles emitted in the transitions from the initial level to this first isomeric level are combined into a first particle batch and started simultaneously in the simulation. Further particle grouping commences with the first isomeric level assuming the role of the initial level and  $n - 1$  remaining potential isomeric levels. If  $t_i < \tau$ , a level  $m$  is searched such that  $\sum_{i=1}^m t_i \geq \tau$ . If such a level exists, all particles emitted in the transitions from the initial level to isomeric level  $m$  are emitted within  $\tau$  and hence started simultaneously in the simulation. Subsequent grouping commences with isomeric level  $m$  assuming the role of the initial level and  $n - m$  remaining potential isomeric levels. If no such level exists, i.e.  $\sum_{i=1}^n t_i < \tau$ , all particles are emitted simultaneously.

## 4. Modeling Data of the Ge Spectrometer TGRS

### 4.1. Instrument and Radiation Environment

The Transient Gamma-Ray Spectrometer (TGRS) on board the *Wind* spacecraft was primarily designed to perform high-resolution spectroscopy of transient  $\gamma$ -ray events, such as  $\gamma$ -ray bursts or solar flares (Owens et al. 1995). The detector itself consists of a 215 cm<sup>3</sup> high purity n-type Ge crystal sensitive to energies in the 20 keV – 8 MeV band, kept at its operating temperature of 85 K by a passive radiative cooler constructed mainly of Be and Mg. Some shielding in the soft X-ray range, mainly against intense solar flare X-rays, is provided by a 30 mil (0.762 mm) thick sheet of Be-Cu alloy around the sides of the cooler. The TGRS detector is located on the south-facing surface of the rotating cylindrical *Wind* body, which points permanently toward the southern ecliptic pole. The spectrometer has no active shielding and is permanently exposed to  $\sim 1.8\pi$  sr of the southern hemisphere which is unobstructed by the cooler. A 1 cm thick Pb occulter attached to the *Wind* body exploits the spacecraft rotation in order to modulate the signal from the ecliptic plane (including the Galactic Center); as seen from the detector it occults a band 90° long by 16° wide sweeping out the whole ecliptic in *Wind's* 3 s rotation period. The chemical elements mentioned, together with Al which was used for most structural components, are expected to be among the main sources of prompt and delayed  $\gamma$ -ray line backgrounds.

Since its launch on November 1, 1994, *Wind* has been following unusual and highly elliptical orbits; halo orbits around the Earth-Sun Lagrangian L1 point in the first half of the mission, trans-lunar Earth orbits in the second half (Acuña et al. 1995). Hence *Wind* spent virtually the whole mission in interplanetary space, well away from near-Earth radiation backgrounds such as geomagnetically trapped particles and Earth albedo radiations. The

radiation environment experienced by TGRS therefore is dominated by two components: diffuse cosmic hard X and  $\gamma$  radiation, and Galactic cosmic rays, unmodulated by the Earth’s magnetic field. Both radiation fields can be considered isotropic. The diffuse cosmic hard X and  $\gamma$  radiation is constant in time. Significant secular changes of Galactic cosmic rays due to solar modulation occur on time scales of a few months. These changes were observed by TGRS in several  $\gamma$ -ray lines (Harris et al. 2001). There have been very few interruptions in the data stream, generally caused by brief passages of the trapped radiation belts around perigee or by triggering of a special mode of data collection by solar flares and  $\gamma$ -ray bursts.

The background spectra recorded by TGRS provide an ideal test for the MGGPOD package. The (relative) simplicity of the instrument design facilitated the development of an accurate model for Monte Carlo simulations (this also applies to the *Wind* spacecraft). The stability and isotropy of the radiation environment, which can be represented by only two dominant components, also greatly simplify Monte Carlo simulations, and at the same time render quantitative comparisons of TGRS spectra with simulations more rigorous. Finally, the fine energy resolution of the detector reveals the plethora of instrumental lines in great detail, providing us with sensitive tests on the numerous interaction channels through which Galactic cosmic rays can deposit their energy in the instrument and spacecraft structures. The resolution of TGRS at 500 keV was nominally about 3 keV full width at half maximum (FWHM), which was achieved in the early months of the mission (Harris et al. 1998); thereafter resolution degraded due to accumulated damage from cosmic-ray impacts (Kurczynski et al. 1999). The line profiles also became distorted, with marked tails on the low-energy wings, and energy calibration became more difficult due to gain shifts. We limit our analysis to the period Jan.–May, 1995, when these problems were negligible, except for small low-energy tails particularly on the highest energy lines (see § 4.3). The TGRS background spectra were binned in 1 keV energy channels over the entire 20 keV – 8 MeV range. However, due to problems with saturation of electronics components after very high energy deposits by heavy Galactic cosmic rays the energy range of TGRS for scientific studies had to be limited to 40 keV – 8 MeV. In addition, the 210–260 keV range is contaminated by electronic artifacts, which appear as broad features in the spectrum. Our reference Jan.–May, 1995 TGRS spectrum is shown in Fig. 5.

The detector cannot distinguish individual energy deposits which occur within the peaking time of the electronics, which is about  $5 \mu\text{s}$ . In general, nuclear transitions within the Ge crystal from excited states to the ground state will be detected at the sum of the energies if they proceed through one or more intermediate levels. An exception occurs for transitions via states with lifetimes  $\tau \gtrsim 5 \mu\text{s}$ , which may survive to be detected separately; we refer to these states as isomers for the purpose of working with TGRS. This is particularly relevant for the de-excitation of  $^{73m}\text{Ge}$ : the de-excitation of the 66.7 keV level ( $\tau = 0.72 \text{ s}$ ) proceeds

via a level at 13.3 keV with  $\tau = 4.3 \mu\text{s}$ . If the 13.3 keV level takes long to de-excite, the decay will be registered as two distinct events, giving rise to lines at 13.3 keV and 53.4 keV; if it de-excites quickly the two photons will be summed giving rise to a single line at 66.7 keV; for intermediate cases the energies are only partially summed and the event will fill in the interpeak region between 53.4 keV and 66.7 keV. Radioactive  $\beta^-$  or  $\beta^+$  decays within the detector do not give rise to line features in the spectrum; the energy of the  $\beta$  particle is distributed continuously and summed with the coincident  $\gamma$  rays of discrete energy. Electron capture  $\beta$  decays within the Ge crystal do produce multiple line features. Electron captures are accompanied by X-rays and/or Auger electrons arising from the filling of a vacancy in one of the atomic sub-shells; lines will appear at the sum of the nuclear transition energy and the binding energy of the atomic sub-shells. Certain lines will appear in the TGRS spectrum which are not due to cosmic-ray effects, notably a strong line at 1460 keV from a  $^{40}\text{K}$  source which was flown for calibration purposes, and lines from the decay chains of U and Th occurring naturally in traces, e.g. in the Be cooler and shield.

## 4.2. Models and Simulation

In modeling the TGRS background by Monte Carlo simulation approximations regarding the mass model representing the instrument and the *Wind* spacecraft, as well as the components of the radiation environment and their time history, are inevitable. All elements of the TGRS instrument described above and of the *Wind* spacecraft are sources of prompt and delayed instrumental backgrounds. The required mass model has to give a faithful representation of the geometrical structure and its atomic/isotopic composition, particularly for the Ge detector and its vicinity. With increasing distance from the detector the details of the mass distribution are less critical; however, we were careful to conserve the total mass of the spacecraft components and to represent their atomic/isotopic composition, as these are important factors for the generation of secondary particles and residual nuclei in hadronic interactions. Our model of the TGRS detector is based on the mass model created by Seifert et al. (1995) for response matrix generation. This early mass model replicated well the geometrical structure and the masses of the TGRS instrument above and around the Ge crystal as described by Owens et al. (1995). However, it did not specify the atomic and isotopic compositions of materials in sufficient detail for our purpose, it did not include instrument components below the Ge crystal, such as electronics boxes, and it only provided the crudest representation of the spacecraft. We supplemented and improved the early TGRS mass model by referring to original technical drawings and other documentation, and by close examination of spare parts. Assuming that the latest documents on the detector mass that were available to us are the most accurate, we can account for about 96% of the mass of

the total instrument (18.1 kg out of 18.9 kg). However, in and close to the detector, i.e. the areas which are most important for the simulation, we can account for only 86% of the material (6 kg out of 7 kg). Our approach to creating a model for the *Wind* spacecraft and other scientific instruments was similar. For example, the basic geometry and structure of the spacecraft body are described in Harten & Clark (1995). We can account for about 86% of the documented spacecraft mass in our mass model.

The radiation environment of TGRS was approximated by its two dominant components: diffuse cosmic hard X and  $\gamma$  radiation, and cosmic radiation. Both were assumed to be isotropic and constant in time. We used an analytic approximation by Gruber et al. (1999) to model the spectrum of the diffuse cosmic photon radiation in the 30 keV to 9 MeV energy range. Due to limitations of GCALOR (see § 3.2) the only hadronic particle component of the cosmic radiation that could be simulated were protons (the contribution of cosmic-ray electrons to TGRS spectra was found to be negligible). We used a proton spectrum (energy range 10 MeV to 226 GeV) that was calculated for early 1995 (Moskalenko 2002, priv. comm.) with the GALPROP Galactic cosmic-ray propagation code, taking into account solar modulation using a steady-state drift model (Moskalenko et al. 2002). The GALPROP code has been shown to reproduce simultaneously observable data of many kinds related to cosmic-ray origin and propagation (Moskalenko & Strong 2000). This model proton spectrum was assumed to be representative of the Jan.–May, 1995 time period, during which the TGRS data we are modeling were recorded. During this time period the activity of some isotopes produced by cosmic radiation built up, and hence their contribution to the TGRS data increased with time. However, the TGRS spectrum we are modeling represents an average over this time period. In our simulations of the instrumental background due to delayed radioactive decays we approximate this time average with a snapshot in March 1995 after four months of cosmic-ray irradiation, i.e. we use isotope activities that are calculated assuming four months of constant irradiation with our model cosmic-ray proton spectrum.

### 4.3. Identifications of TGRS Instrumental Lines

One of the main goals for developing the MGGPOD suite was to create a Monte Carlo tool capable of modeling the many instrumental lines present in  $\gamma$ -ray detectors. To assess the extent to which this goal was reached for TGRS we attempted to identify its more than 200 observable lines and spectral features. The TGRS spectra were analyzed using the GAS-

PAN<sup>12</sup> gamma spectrum analysis program. GASPAN allowed us to characterize the shape of the instrumental lines as a function of energy, following parametrizations given by Phillips & Marlow (1976). The photopeak component of each line was described by a Gaussian and a low-energy “wing”, whose importance increased with energy. The wing was modeled by the sum of two exponential tails representing effects from multiple Compton scatterings and incomplete charge collection. The line width and tail parameters were determined as a function of energy using the strongest and cleanest lines. This energy dependent line shape was then employed to analyse TGRS spectra, particularly to resolve the many closely spaced or blended lines. When analyzing intrinsically broad lines arising from the prompt de-excitation of very short-lived levels ( $T_{1/2} \lesssim 0.5$  ps, Evans et al. 2002) allowance had to be made for their exceptional width, which is caused by Doppler broadening due to the motion of the nucleus during de-excitation.

The results of our spectral analysis are summarized in Tables 5 and 6, in which the lines are identified and the count rates in the observed spectrum are presented. Lines or blended features for which the GASPAN fit determined a significance  $< 5\sigma$  are not included. Most of the strong lines had already been identified with nuclear transitions in previous work with Ge spectrometers (Wheaton et al. 1989; Bartlett 1994; Evans et al. 2002; Weidenspointner et al. 2003), with which our results are in general agreement. However, the level of detail with which our simulation was performed allowed us to suggest that in many cases multiple transitions can be identified contributing to previously unidentified blends. Thus in Tables 5 and 6 two or more transitions are frequently assigned to an observed line feature. The order in which the transitions are listed corresponds to their ranking as contributors to the line strength, according to the simulation, with transitions whose contribution was  $< 10\%$  according to the simulation being omitted. Table 7 lists identified triangular or “sawtooth” shaped features from inelastic neutron scattering off Ge nuclei in the detector crystal, as described in § 3.3.1.

Narrow (unresolved) lines were assigned to Table 5 if one or more identifications could be made, from earlier work or from the simulation. If no certain identification could be made they were put in Table 6, whose purpose is to draw attention to gaps in our knowledge of nuclear physics to encourage further work. Lines which were visibly broader than the TGRS energy resolution were treated as blends, keeping in mind that an intrinsically broad component might also contribute. If multiple identifications were possible, sufficient (in theory) to explain the line width, the line was included in Table 5. Two indications were

---

<sup>12</sup>The software, developed by F. Riess, and documentation are available under <http://ftp.leo.org/download/pub/science/physics/software/gaspan/>; alternatively, F. Riess can be contacted directly (friedrich@die-riessens.de)

used to assign a blend to the “uncertain identity” category (Table 6). First, a blend which was obviously broad enough to contain multiple lines might correspond to only one line in the simulation (or none). Second, a comparison of the observed and predicted line strengths might show the simulation seriously failing to reproduce an observed line. Although there is considerable scatter in the reliability of the simulations even for well-identified narrow lines (see below), we somewhat arbitrarily assigned blends where the ratio of simulated to observed line strength fell below 25% to Table 6.

There are some obvious deficiencies in this qualitative procedure by which Tables 5 and 6 were compiled. There are considerable quantitative uncertainties in the simulations, as we shall see, preventing the ranking of transitions and the 10% cutoff from being totally reliable. The simulation may even omit lines altogether. Such cases belong in Table 6, but may appear in Table 5 if the line appears narrow or if  $> 25\%$  of its observed strength is predicted by the simulations. Several cases of this kind may be indicated by measurements of the line energy in Table 5 which are inconsistent with the transition energies. However, these cases may also be due to problems inherent in the use of the rather complicated function (Phillips & Marlow 1976) for fitting the line profiles.

#### 4.4. Comparison of Simulation and Data

A comparison of the overall Jan.–May, 1995 TGRS spectrum with the various components of our MGGPOD simulation is shown in Fig. 5. The simulated instrumental background components are: prompt background due to cosmic-ray proton interactions and prompt de-excitations (green), delayed backgrounds from radioactive decays in the TGRS instrument and the *Wind* spacecraft (purple), and background due to diffuse cosmic X and  $\gamma$  rays (blue). The sum of all components is depicted in red, and the data are shown in black (the broad features in the 210–260 keV region are electronic artifacts). For better comparison, a model of the instrumental resolution has been applied to the simulation results. This model includes the anomalous width of the 511 keV line, which arises from the finite momenta of positron and electron at annihilation, but does not include Doppler broadening of lines due the motion of the nucleus during de-excitation from short-lived levels with  $T_{1/2} \lesssim 0.5$  ps (Evans et al. 2002), as is the case e.g. for the 4438 keV line from  $^{12}\text{C}^*$ . Lines due to radio-isotopes of the so-called natural decay chains (e.g.  $^{212}\text{Pb}$ ) and due to the  $^{40}\text{K}$  calibration source are not included in the simulations. Comparisons of the Jan.–May, 1995 TGRS spectrum in smaller energy ranges with the summed MGGPOD simulation are provided in Figs. 6–10. In these figures, some of the more prominent lines and spectral features have been labelled for easier reference to the detailed identifications in Tables 5 and 6.

#### 4.4.1. *Continuum and Inelastic Neutron Scattering Features*

The MGGPOD simulation reproduces very well the overall shape and magnitude of the actual background. This is illustrated in Fig. 11, which depicts the ratio between the simulation and the measured spectrum. Disregarding line features, this ratio exhibits very little trend with energy and has a value of about 0.85. The only exception occurs at the lowest energies, below about 200 keV, where the ratio increases with decreasing energy up to a value of 1.2.

Below about 200 keV diffuse cosmic photons are found to be the dominant source of instrumental background in TGRS, as expected for a wide field-of-view instrument. Prompt cosmic-ray proton induced events are the main background component at energies above about 200 keV, and practically the sole background above about 4 MeV. The relative dominance of the prompt background in TGRS reflects the lack of any veto shielding. The prompt background comprises different processes, among them direct ionization in the detector by cosmic-ray protons and energy losses by secondaries, including energy deposits due to elastic and inelastic scattering of secondary neutrons off Ge nuclei in the detector crystal. The prompt background is not a pure continuum, but features numerous lines; these will be addressed in § 4.4.2.

As discussed in § 3.3.1, inelastic neutron scattering gives rise to characteristic “saw-tooth” or triangular-shaped broad features in the spectrum. Their absolute and relative strengths, and less so their detailed shape, are sensitive to the flux and spectral distribution of secondary neutrons in the Ge crystal at energies around 1 MeV. In Table 7 we attempt to make comparisons between our measurements of the triangular inelastic neutron scattering features and the simulations. Fig. 5, and in more detail Figs. 6–8, make it clear that upon these features there are superposed a large number of strong lines, that underlying them there must be a continuum of somewhat uncertain shape, and that the features sometimes overlies each other. Nevertheless, there is sufficient resemblance between the simulated and observed recoil features for comparisons to be made – lower and higher energy bounds and lines can be consistently identified, hence simulation and observation can be treated consistently.

Our method involved simply identifying the lower and upper energy bounds of the recoil features, summing the counts between these limits, and subtracting the estimated counts contributed by the lines and the continuum. The uncertainties in the values in Table 7 are overwhelmingly dominated by the uncertainties in the true values of line and continuum count rates. We quote ranges of count rate in each recoil feature corresponding to the most extreme estimates of the line and continuum strengths. The extreme low continuum estimate assumes a flat continuum having the flux corresponding to the upper energy bound; the high continuum estimate is a linear interpolation between the lower and higher energy bounds.

The line measurements within the recoil feature energy ranges (Table 5) were assumed to be upper limits because of the possibility of contamination by the recoil feature. Of course, upper line and continuum limits correspond to lower limits on the strength of the recoil feature in Table 7, and *vice versa*.

In Table 7, note that the upper and lower energy bounds are somewhat arbitrarily chosen from one feature to the next, due to the interference of strong lines and other recoil features. Thus the results should not be compared from one feature to the next – the important point is that theory and observation can be compared within the same feature, since they are treated consistently.

We are left with the conclusion, based on the figures in Table 7 (where comparable) that the simulation and the measurement in general agree within 30% – an exception is the one above 834 keV, which suffers exceptionally strong interference from the lines at 844 and 847 keV (see Fig. 7). This estimate is supported by the lack of any discontinuities in the ratio of simulation and actual data at the recoil features’ energy ranges in Fig. 11. There is a weak tendency for the theory to over-predict the strength of the recoil features. This might result from systematic errors in any of the various quantities that are relevant for the simulation of the recoil features, such as the flux of secondary neutrons – which depends e.g. on the accuracy of the mass model and of hadronic cross-sections in general, and the Ge neutron cross-sections in particular.

Delayed radioactive decays in the TGRS instrument and the *Wind* spacecraft also give rise to continuum background ( $\gamma$ -ray lines from radioactive decays are discussed below). The dominant contributors are  $\beta$  decays in the Ge crystal. As described in § 4.1,  $\beta^-$  or  $\beta^+$  decays within the Ge detector result in a pure continuum background (except if isomeric levels are involved in the de-excitation of the daughter nucleus) because the continuously distributed energy of the  $\beta$  particle is summed with the coincident  $\gamma$  rays of discrete energy. In the case of TGRS and *Wind*, continuum background due to radioactive decays in the spacecraft is relatively less important because  $m/r^2$ , with  $m$  being a mass element and  $r$  the distance from the detector, is lower for the spacecraft structure than for instrument parts. The delayed background exceeds the diffuse cosmic photon background above about 400 keV, and cuts off at about 4 MeV.

#### 4.4.2. Lines

The simulation is also very successful in modeling the more than 200 lines that are observed in the TGRS spectrum. Most (about 87%) of the lines are reproduced, with the

ratio of simulated and actual line count rates clustering around a value of 1 with no trend in energy. The simulation produces a few spurious lines, and fails to reproduce a few lines that are present in the data.

A quantitative comparison of simulated and observed line strengths is shown in Fig. 12, in the form of a scatter plot of the ratio between them as a function of line energy. The distribution of the numerical values of these ratios are shown in Fig. 13. Overall, the observed lines are reproduced within a factor  $\sim 2.5$ . There is no trend with energy in Fig. 12, and the mean ratio is very close to 1, suggesting that our methods of line simulation (§§ 3.5, 3.3) are sound to a first level of approximation. There are enough lines (205) for the results to be broken down into subsets in search of interesting systematic deviations from these overall conclusions.

If the simulated-to-observed line strength ratios are broken down by reaction type it is found that lines from radioactive decays are on average well reproduced by the simulation, while spallation reaction line strengths are somewhat overestimated (Fig. 13, dotted line). Leaving aside possible problems of isotope production from the incoming channel cross-sections in GCALOR, this effect results solely from a systematic overestimate of the strengths of lines from low-mass ( $20 \leq A \leq 30$ ) nuclei, by a factor of nearly 2 (Fig. 13, dashed line). This indicates that the thermal approximation for spallation product de-excitations (§ 3.3) becomes increasingly inadequate with decreasing mass number below  $A = 30$ , as might be expected from nuclear level statistics. Spallation reactions overall do not show a wider spread than the others (a factor  $\sim 2.5$  in Fig. 13), nor do they show any trend with line energy. This indicates that, to the extent that the thermal approximation is valid, the choice of temperature 3 MeV is justified.

## 5. Summary and Conclusion

We have described the capabilities, functioning, and structure of the MGGPOD Monte Carlo simulation suite, which is based on the widely used GEANT Detector Description and Simulation Tool (Version 3.21, Brun et al. 1995). MGGPOD is a user-friendly simulation package that is applicable to all stages of space-based  $\gamma$ -ray astronomy missions. In particular, the MGGPOD package allows *ab initio* simulations of instrumental backgrounds, both continuum and  $\gamma$ -ray lines, that arise from interactions of the various radiation fields within the instrument and spacecraft materials. It is possible to simulate both prompt instrumental backgrounds, such as energy losses of cosmic-ray particles and their secondaries, as well as delayed instrumental backgrounds, which are due to the decay of radioactive isotopes produced in nuclear interactions. The MGGPOD package and documentation

are available to the public for download at the Centre d’Etude Spatiale des Rayonnements (<http://sigma-2.cesr.fr/spi/MGGPOD/>).

To demonstrate its capabilities, we employed the MGGPOD suite for modeling high resolution  $\gamma$ -ray spectra recorded by the Transient Gamma-Ray Spectrometer (TGRS) on board *Wind* during 1995. We found that both the continuum and the  $\gamma$ -ray line background are very well reproduced. Regarding the continuum background, the ratio between simulation and flight data is about 0.85, except for the lowest energies below about 200 keV, where the ratio increases with decreasing energy up to a value of 1.2. The simulation even reproduces well asymmetric, “sawtooth” or triangular-shaped broad spectral features that are due to inelastic neutron scattering off Ge nuclei in the detector. Regarding background lines, the simulation reproduces about 87% of the observed background lines in TGRS, with the ratio of simulated and actual line count rates clustering around a value of 1 with no trend in energy. Our results for continuum and lines are as good as or better than those obtained by Dyer et al. (1994) for OSSE, by Dyer et al. (1998) for *Mars Observer*, or Graham et al. (1997) for *HEAO-3* using other Monte Carlo tools.

Below about 200 keV, diffuse cosmic photons are found to be the dominant source of instrumental background in TGRS. The simulation overestimates this component, with the largest deviation of 20% occurring at the lowest energies. We attribute the overestimate mainly to uncertainties in the mass distribution around the Ge detectors. Although we made a substantial effort to describe the detector as accurately as possible in our mass model, we may have missed material in and close to the detector (as described in § 4.2). Small changes in the amount and distribution of mass close to the detector have a large effect on the simulated count rate at a few tens of keV because of the strong photoelectric absorption at these energies, and also affect the probability of Compton scattering of higher-energy photons into the detector. As mentioned in § 4.2, we employed in our simulations an analytical model of Gruber et al. (1999) for the spectrum of the diffuse cosmic photons, which was obtained by fitting results from various instruments. The uncertainty of this model is expected to be smaller than our overestimate of the background due to diffuse cosmic photons; hence the model is unlikely to be the sole cause of it.

The shortfall of the simulation above 200 keV is expected. Currently, GCALOR is not capable of simulating hadronic interactions of  $\alpha$  particles, hence the contributions of cosmic-ray  $\alpha$  particles to the prompt and the delayed background could not be modeled. A rough estimate of this contribution can be obtained with an empirical formula for the ratio of the total  $\alpha$  to proton cross-sections by Ferrando et al. (1988). This ratio does not vary much with the mass of the target nucleus between Al and Ge, and has an average value of about 1.7. By number, the ratio of cosmic-ray  $\alpha$ s to protons is about 0.14; hence we can estimate that

if cosmic-ray  $\alpha$  particles could be included in the simulation, they would increase the prompt and delayed background by roughly 24% – enough to account for the current short-fall of about 15%. The effect of  $\alpha$  induced spallations on the activation of specific isotope species is very difficult to estimate, since the ratio of  $\alpha$  to proton cross-sections for specific spallation products strongly varies with energy (Ferrando et al. 1988). Similarly, when modeling data from the OSSE instrument on board *CGRO*, Dyer et al. (1994) concluded that  $\alpha$  particles account for about 20% of the calculated activation due to cosmic rays. In addition, there are deficiencies in the mass model, since the total mass accounted for in the instrument and the spacecraft falls short of the documented mass budget by about 14% (§ 4.2). Less mass will result in fewer interactions and hence less prompt background as well as less activation and therefore less delayed background. Except for the lowest energies, shielding of the detector from  $\gamma$ -rays originating in different parts of the detector and spacecraft is not expected to be significantly affected by the moderate mass deficit.

The simulation reproduces about 87% of the observed background lines in TGRS, with the ratio of simulated to measured line count rates clustering around a value of 1 with no trend in energy. On average, lines from radioactive decays are well reproduced. We see a small trend of overproduction for lines from de-excitation of spallation products with decreasing mass. This trend is expected given the simple statistical method that is used for generating de-excitation photons.

The simulation of lines from de-excitations involving isomeric levels is influenced by the choice for the detector time constant (§ 4.1). In our simulations, we set this parameter to  $\tau = 5 \mu\text{s}$ ; hence the results for lines from the isomeric levels of  $^{73}\text{Ge}$  (the 13.3 keV level has a lifetime of 4.3  $\mu\text{s}$ ) are particularly sensitive to this parameter. As can be seen in Figs. 5, 6, and 11, both lines at 53.4 keV and 66.7 keV are overestimated, with the sum peak being relatively too strong. In the simulation, partial summation of energy deposits by the electronics, which fills the interpeak region, is not modeled, thereby overestimating the sum peak. However, to reproduce the shape of the  $^{73m}\text{Ge}$  complex better in the simulation, the parameter  $\tau$  needs to be set to a value smaller than 5  $\mu\text{s}$ .

There are a few lines which allow us to assess the overall quality of the simulation. The 511 keV line, which results from a multitude of processes (e.g. decay of  $\pi^+$  produced in hadronic interactions, electromagnetic showers, radioactive decays) is reproduced within a factor of 0.74, indicating that there are no severe problems with modeling the diverse physics involved. The 2.223 MeV line from thermal neutron capture on H, the features from inelastic neutron scattering off Ge, and the Doppler broadened line at 2.211 MeV line from inelastic neutron scattering on  $^{27}\text{Al}$  are reproduced within factors of 1.4,  $\lesssim 1.3$ , and 1.1, respectively. This indicates that flux and energy spectrum of secondary neutrons throughout TGRS and

*Wind* are fairly well reproduced, which in turn implies that there are no severe problems with the treatment of neutron production, propagation, and interaction.

The remarkable performance of MGGPOD in modeling TGRS data encouraged us and others to employ this Monte Carlo suite to other instruments. Preliminary results for the spectrometer SPI on board *INTEGRAL* have been reported by Weidenspointner et al. (2004a). MGGPOD reproduces well early-mission SPI data; however, remaining discrepancies imply that in the case of this much heavier and complex mission (compared to TGRS) there are deficiencies in the production and/or thermalization and capture of secondary neutrons. This has lead us to an ongoing systematic evaluation of the neutron cross-sections in GCALOR, whose results will be presented in a future publication of a re-visited SPI background simulation. Recently, MGGPOD has also been applied to *RHESSI* by Wunderer, Smith, & Weidenspointner (2004). These preliminary results are encouraging, the overall spectrum is well reproduced. As expected for a mission in low-Earth orbit (e.g. Weidenspointner et al. 2001), the background is dominated by decays of radioactive isotopes produced during SAA passages. However, both SAA induced continuum and line components are overproduced, indicating the need for refining the modeling of the time-dependent activation during SAA passages. Two of us (G. W. and M. J. H.) will use MGGPOD to estimate instrumental background and sensitivity of the space based gamma-ray lens MAX (von Ballmoos et al. 2004). The performance and user-friendliness of MGGPOD also attracted the various instrument teams studying concepts for an advanced Compton telescope; they selected MGGPOD as their baseline simulation tool for predicting the performance and sensitivity of the various designs. To address better the requirements for studying the performance of these complex instruments, Version 1.1 of MGGPOD, which is currently under development, will provide additional beam geometry and spectral options, will include the capability of modeling polarized photons, and will support additional output formats suitable for the advanced event reconstruction algorithms (e.g. Zoglauer, Andritschke, & Kanbach 2004) that are foreseen for these instruments.

We are grateful to David Palmer, Helmut Seifert, and Juan Naya for helpful discussions about the TGRS instrument. We are indepted to Prof. Friedrich Riess for enhancing GASPAN according to our needs, and for user support.

## REFERENCES

- Acuña, M. H., Ogilvie, K. W., Baker, D. N., Curtis, S. A., Fairfield, D. H., & Mish, W. H. 1995, *Space Sci. Rev.*, 71, 5

- Bartlett, L. M. 1994, PhD thesis, University of Maryland
- Blatt, J. M., & Weisskopf, V. F. 1952, *Theoretical Nuclear Physics*, New York, Wiley
- Brun, R. 1995, *GEANT Detector Description and Simulation Tool*, CERN Program Library Long Writeup W5013, available at <http://wwwinfo.cern.ch/asd/geant/>
- Bunting, R. L., & Kraushaar, J. J. 1974, *Nuclear Instruments and Methods*, 118, 565
- Dean, A. J., Lei, F., & Knight, P. J. 1991, *Space Sci. Rev.*, 57, 109
- Dean, A. J., Bird, A. J., Diallo, N., Ferguson, C., Lockley, J.J., Shaw, S. E., Westmore, M. J., & Willis, D. R. 2003, *Space Sci. Rev.*, 105, 285
- Diallo, N., Shaw, S., Dean, A. J., Ferguson, C., Perfect, C., & Weidenspointner, G. 2001, in *Exploring the Gamma-Ray Universe* (ESA SP-459), 561
- Dyer, C. S., Truscott, P. R., Evans, H. E., Hammond, N., Comber, C., & Battersby S. 1994, *IEEE Transactions on Nuclear Science*, 41, 438
- Dyer, C., Truscott, P., Evans, L., & Trombka, J. 1998, in *Conference on the High Energy Radiation Background in Space (CHERBS) 1997*, 53
- Evans, L. G., Boynton, W. V., Reedy, R. C., Starr, R. D., & Trombka, J. I. 2002, in *Hard X-Ray and Gamma-Ray Detector Physics IV* (SPIE Conference 4784), ed. R. B. James, L. A. Franks, A. Burger, E. M. Westbrook, & R. D. Durst, 31
- Ferrando, P., Webber, W. R., Goret, P., Kish, J. C., Schrier, D. A., Soutoul, A., & Testard, O. 1988, *Phys. Rev. C*, 37, 1490
- Firestone, R. B. 1996, *Table of Isotopes* (8<sup>th</sup> Edition), Wiley & Sons, Inc.
- Gabriel, T. A., et al. 1995, *CALOR95: A Monte Carlo Program Package for the Design and Analysis of Calorimeter Systems*, ORNL/TM-11185
- Galín, J. 2001, *Pramana*, 57, 67
- Gehrels, N. 1985, *Nuc. Instr. and Meth. in Phys. Res. A*, 239, 324
- Gehrels, N. 1992, *Nuc. Instr. and Meth. in Phys. Res. A*, 313, 513
- Graham, B. L., Philips, B. F., Kroeger, R. A., & Kurfess, J. D. 1997, in *Proc. of the Fourth Compton Symposium* (AIP 410), 1642
- Gruber, D. E., Matteson, J. L., Peterson, L. E., & Jung, G. V. 1999, *ApJ*, 520, 124

- Harris, M. J., Teegarden, B. J., Cline, T. L., Gehrels, N., Palmer, D. M., Ramaty, R., & Seifert, H. 1998, *ApJ*, 501, L55
- Harris, M. J., Teegarden, B. J., Weidenspointner, G., Palmer, D. M., Cline, T. L., Gehrels, N., & Ramaty, R. 2001, *ApJ*, 563, 950
- Harris, M. J., Share, G. H., & Leising, M. D. 2003, *J. Geophys. Res.*, 108(A12), 1435
- Harten, R., & Clark, K. 1995, *Space Sci. Rev.*, 71, 23
- Holmes, J. A., Woosley, S. E., Fowler, W. A., & Zimmermann, B. A. 1976, *Atomic Data Nucl. Data Tables*, 18, 305
- Johnson, J. O., & Gabriel, T. A. 1987, *Development and Evaluation of a Monte Carlo Code System for Analysis of Ionization Chamber Response*, ORNL/TM-10196
- Johnson, J. O., & Gabriel, T. A. 1988, *A User's Guide to MICAP: A Monte Carlo Ionization Chamber Analysis Package*, ORNL/TM-10340
- Kinzer, R. L., Jung, G. V., Gruber, D. E., Matteson, J. L., & Peterson, L.E. 1997, *ApJ*, 475, 361
- Kippen, R. M. 2002, *GEANT Low-Energy Compton Scattering (GLECS) package*, available at <http://nis-www.lanl.gov/~mkippen/actsim/glecs/>
- Kippen, R. M. 2004, *New Astronomy Reviews*, 48, 221
- Klecker, B. 1996, *Adv. Space Res.*, 17(2), 37
- Kurczynski, P., et al. 1999, *Nuc. Instr. and Meth. in Phys. Res. A*, 431, 141
- Kurfess, J. D., Share, G. H., Kinzer, R. L., Johnson, W. N., Adams, J. H., Jr. 1989, in *High-Energy Radiation Background in Space (AIP 186)*, 250
- Ledoux, X., et al. 1998, *Phys. Rev. C*, 57, 2375
- Lei, F., Green, A. R., Bird, A. J., & Dean, A. J. 1996, in *Environment Modelling for Space-based Application (ESA SP-392)*, 97
- Morris, D. J., et al. 1998, *Adv. Space Res.*, 21/12, 1789
- Moskalenko, I. V., & Strong, A. W. 2000, *Ap&SS*, 272, 247
- Moskalenko, I. V., Strong, A. W., Ormes, J. F., & Potgieter, M. S. 2002, *ApJ*, 565, 280

- Mughabghab, S. F., & Dunford, C. L. 1998, in *Proc. of the International Conference on the Physics of Nuclear Science and Technology*, Vol. 1, 784, also available at <http://www.nndc.bnl.gov/nndc/lvlden/BNL-65712.HTML>
- Naya, J. E., Jean, P., Bockholt, J., von Ballmoos, P., Vedrenne, G., & Matteson, J., 1996, *Nuc. Instr. and Meth. in Phys. Res. A*, 368, 832
- Owens, A., et al. 1995, *Space Sci. Rev.*, 71, 273
- Phillips, G. W., & Marlow, K. W. 1976, *Nucl. Instr. Methods*, 137, 525
- Ramaty, R., Kozlovsky, B., & Lingenfelter, R. E. 1979, *ApJS*, 40, 487
- Seifert, H., et al. 1995, *Gamma-Ray Bursts* (AIP 384), 258
- Smith, D. L. 1972, *Nucl. Instr. Methods*, 102, 193
- Smith, D.M., et al., *Solar Physics* 210, 33, 2002
- Sreekumar, P, et al. 1998, *ApJ*, 494, 523
- Stassinopoulos, E. G. 1989, in *High-Energy Radiation Background in Space* (AIP 186), 3
- Sturmer, S., Seifert, H., Shrader, C., & Teegarden, B. J. 2000, *The Fifth Compton Symposium* (AIP 510), 814
- Sturmer, S., et al. 2004, *A&A*, 411, L81
- Thompson, D. J., & Simpson, G. A., *J. Geophys. Res.*, 86(A3), 1265
- von Ballmoos, P., et al. 2004, *Proc. of SPIE*, Vol. 5168, 482
- Weidenspointner, G., et al. 1996, *A&AS*, 120, 631
- Weidenspointner, G., et al. 2000, *Proc. of 5th Compton Symposium* (AIP 510), 467
- Weidenspointner, G., et al. 2001, *A&A*, 368, 347
- Weidenspointner, G., & Varendorff, M. 2001, in *The Universe in Gamma-Rays*, Springer, 339
- Weidenspointner, G., Harris, M. J., Jean, P., & Diallo, N. 2002, *New Astronomy Reviews*, 46, 625
- Weidenspointner, G., et al. 2003, *A&A*, 411, L113

- Weidenspointner, G., Harris, M. J., Ferguson, C., Sturmer, S., & Teegarden, B. J. 2004a, *New Astronomy Reviews*, 48, 227
- Weidenspointner, G., Harris, M. J., Ferguson, C., Sturmer, S., Teegarden, B. J., & Wunderer, C. 2004b, in *Proc. of 5<sup>th</sup> INTEGRAL workshop*, in press
- Weisskopf, V. F., & Ewing, D. H. 1940, *Phys. Rev.*, 57, 472
- Whatts, J. W., Parnell, T. A., & Heckman, H. H. 1989, in *High-Energy Radiation Background in Space* (AIP 186), 75
- Wheaton, W. A., Jacobson, A. S., Ling, J. C., Mahoney, W. A., & Varnell, L. S. 1989, *High Energy Radiation Background in Space* (AIP Proc. 186), ed. A. C. Rester, Jr., & J. I. Trombka (New York: AIP), 304
- Wunderer, C., Smith, D.M., & Weidenspointner, G., in *Proc. of 5<sup>th</sup> INTEGRAL workshop*, in press
- Zeitnitz, C., & Gabriel, T. A. 1994, *NIM A* 349, 106
- Zeitnitz, C., & Gabriel, T. A. 1999, *The GEANT-GCALOR Interface User's Guide*, available from <http://wswwww.physik.uni-mainz.de/zeitnitz/gcalor/gcalor.html>
- Zoglauer, A., Andritschke, R., & Kanbach, G. 2004, *New Astronomy Reviews*, 48, 231

Fig. 1.— A flow chart illustrating the overall structure of the MGGPOD Monte Carlo simulation suite. The various simulation packages (shown in boxes) and input and output files (shown in ellipses and round-edged boxes) are explained in the text.

Fig. 2.— Schematic representation of our treatment of  $(n,\gamma)$  reactions. The incoming neutron (left, bold arrow) is captured in a level at excitation energy  $S_n + E_k$  in the compound nucleus, where  $S_n$  is the neutron separation energy and  $E_k$  the neutron’s kinetic energy. Spin  $\sigma$  and parity  $\pi$  are assigned to this level using the level density formula of Mughabghab & Dunford (1998) to obtain a random value (inset (a)). In the general case the level is then allowed to decay electromagnetically to known levels of the nucleus (arrows down) which have compatible spin and parity according to the electric dipole selection rules; the probability of transition to any level is proportional to  $E_\gamma^3$ . In the special case (b), where the  $J^\pi$  of the excited level are compatible with s-wave neutron capture, the downward transition probabilities are obtained directly from measured thermal neutron capture data (ENSDF).

Fig. 3.— Schematic representation of our treatment of neutron inelastic scattering. The excitation produced in the target nucleus is known from the GCALOR particle tracking. Two cases arise. (a) The incoming neutron (left, bold arrow) excites a level in the target which lies above the highest known level  $E_h$ . The excited level is assigned a spin and parity at random from the level density distribution (curve inset, top right). The level density formula is evaluated at energy  $E_{ref} \sim 10$  MeV, approximately where the inelastic cross-section peaks. A de-excitation transition is assigned to the highest known level with  $J^\pi$  compatible with an E1 transition (dashed arrow). (b) The incoming neutron deposits energy of a known level (or between known levels); the nearest level in energy is assumed to be excited. In either case, once a known level has been occupied the cascade of transitions down to the ground state is taken from the ENSDF database.

Fig. 4.— Schematic representation of our treatment of spallation reactions. The incoming particle (left, bold arrow) at very high energies leaves the compound nucleus in a thermal distribution of excited states which loses energy by particle emission. When it has lost enough energy that only a small "tail" remains above the neutron separation energy  $S_n$ , particle emission ceases. The thermal distribution function shown at right (rotated) then applies (the "tail" being shaded), and the known levels (full) in the remnant nucleus are populated according to a temperature  $T = 3$  MeV. De-excitations from these known levels (an example at energy  $U_x$  is shown) are then taken from the ENSDF nuclear database. We do not consider the unknown levels (dash) because there are no data for them in ENSDF.

Fig. 5.— A comparison of the overall Jan.–May, 1995 TGRS spectrum with the various components of our MGGPOD simulation. Details are given in the text. The broad features

in the data in 210–260 keV are electronic artifacts.

Fig. 6.— A comparison of the Jan.–May, 1995 TGRS spectrum in 40–800 keV with the summed MGGPOD simulation. Some of the more prominent lines and spectral features have been labelled, including the inelastic neutron scattering features corresponding to the 596 keV and 692 keV levels of  $^{74}\text{Ge}$  and  $^{72}\text{Ge}$ , respectively.

Fig. 7.— A comparison of the Jan.–May, 1995 TGRS spectrum in 800–1100 keV with the summed MGGPOD simulation. Some of the more prominent lines and spectral features have been labelled, including the inelastic neutron scattering features corresponding to the 834 keV and 1039 keV levels of  $^{72}\text{Ge}$  and  $^{70}\text{Ge}$ , respectively.

Fig. 8.— A comparison of the Jan.–May, 1995 TGRS spectrum in 1100–1900 keV with the summed MGGPOD simulation. Some of the more prominent lines and spectral features have been labelled, including the inelastic neutron scattering features corresponding to the 1204 keV and 1215 keV levels of  $^{74}\text{Ge}$  and  $^{70}\text{Ge}$ , respectively.

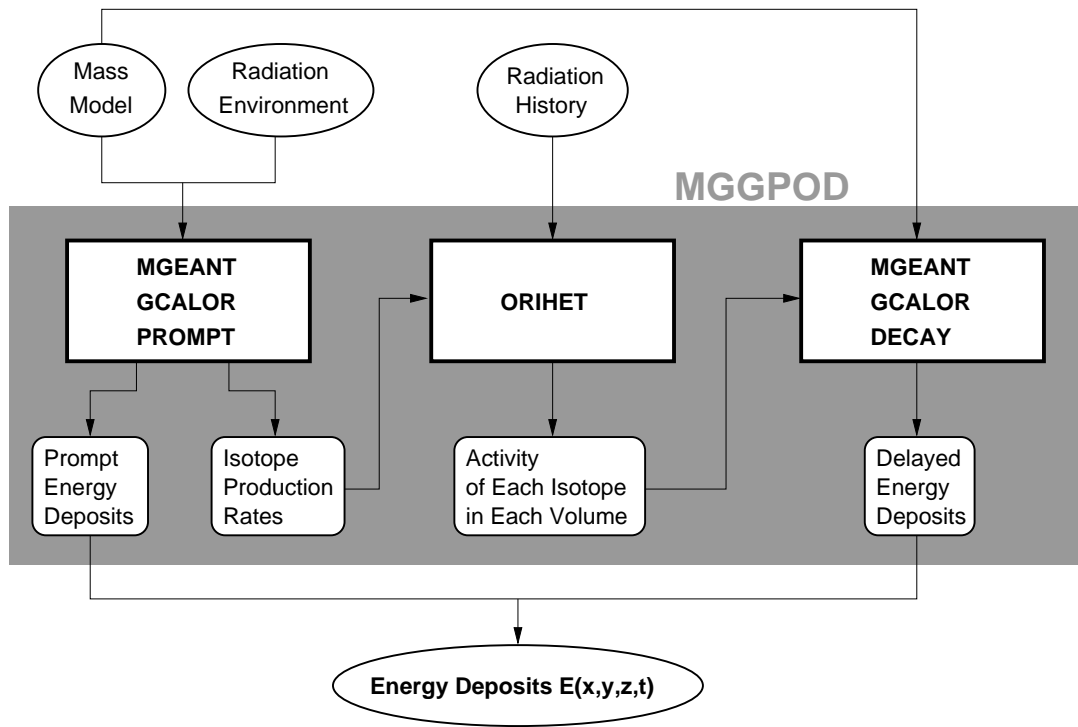
Fig. 9.— A comparison of the Jan.–May, 1995 TGRS spectrum in 1900–3200 keV with the summed MGGPOD simulation. Some of the more prominent lines and spectral features have been labelled.

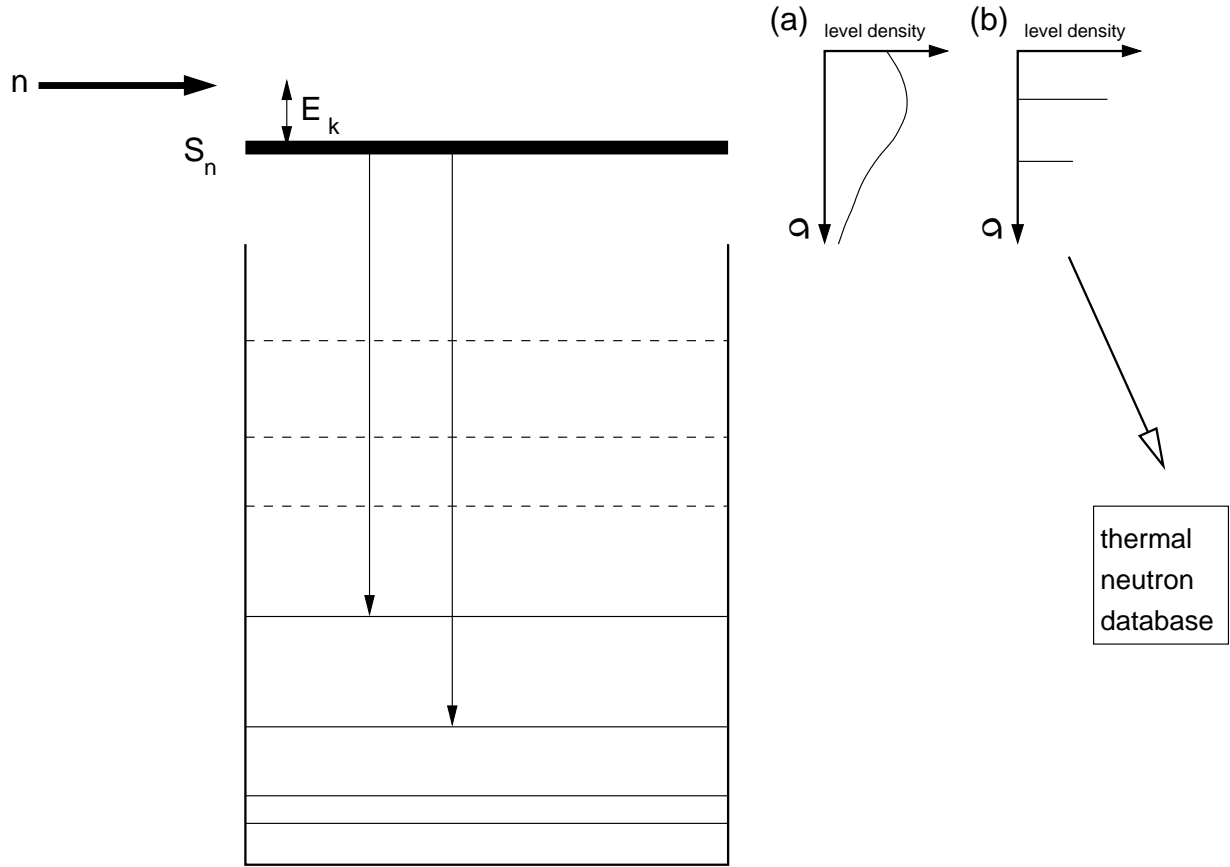
Fig. 10.— A comparison of the Jan.–May, 1995 TGRS spectrum in 3200–8000 keV with the summed MGGPOD simulation. Some of the more prominent lines and spectral features have been labelled. The Doppler broadening of e.g. the  $^{12}\text{C}^*$  lines is not included in the simulation.

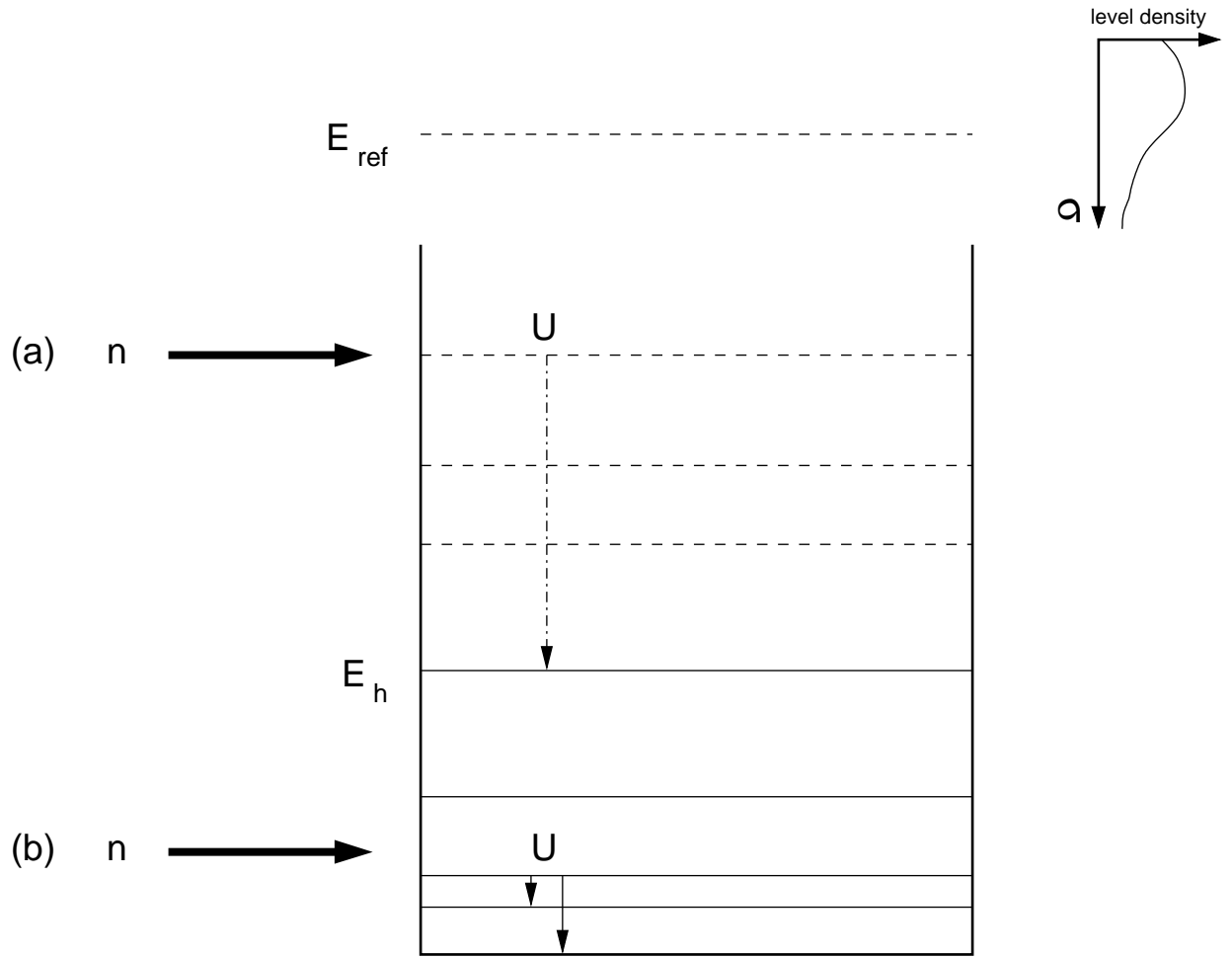
Fig. 11.— The ratio of the MGGPOD simulation and the Jan.–May, 1995 TGRS spectrum.

Fig. 12.— Ratio between simulated and observed line strengths for TGRS background spectrum accumulated during Jan.–May, 1995. Top arrows – lines predicted by simulation but not observed. Bottom arrows – observed lines without simulated equivalents (mostly from  $A < 20$  spallation product nuclei not included in simulation). The lines are well reproduced, typically to within a factor of 2.5.

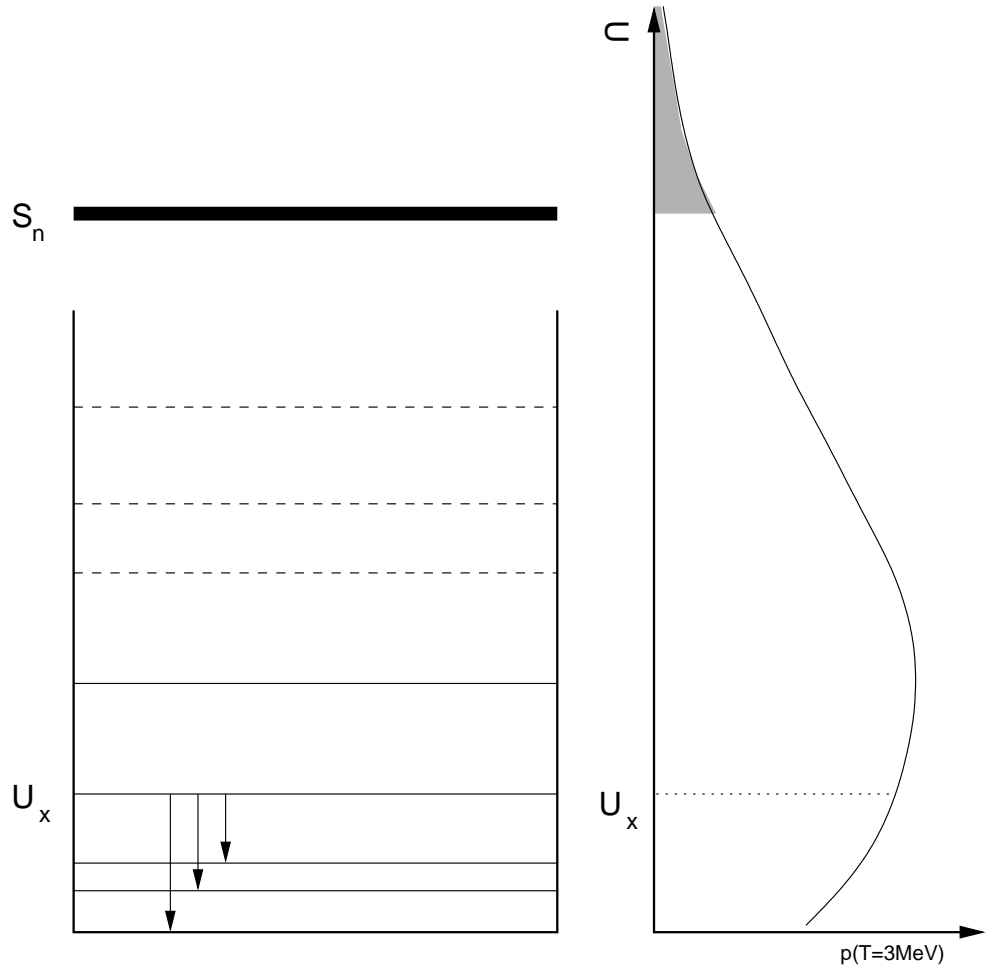
Fig. 13.— Distribution of ratios of simulated to observed line strengths. Full histogram – all lines. Dotted histogram – de-excitation lines from spallation reactions. Dashed histogram – de-excitation lines from spallation reactions yielding nuclei with mass  $20 \leq A \leq 30$ . The symbol “>>” indicates the bin containing lines predicted but not observed (infinite ratio).

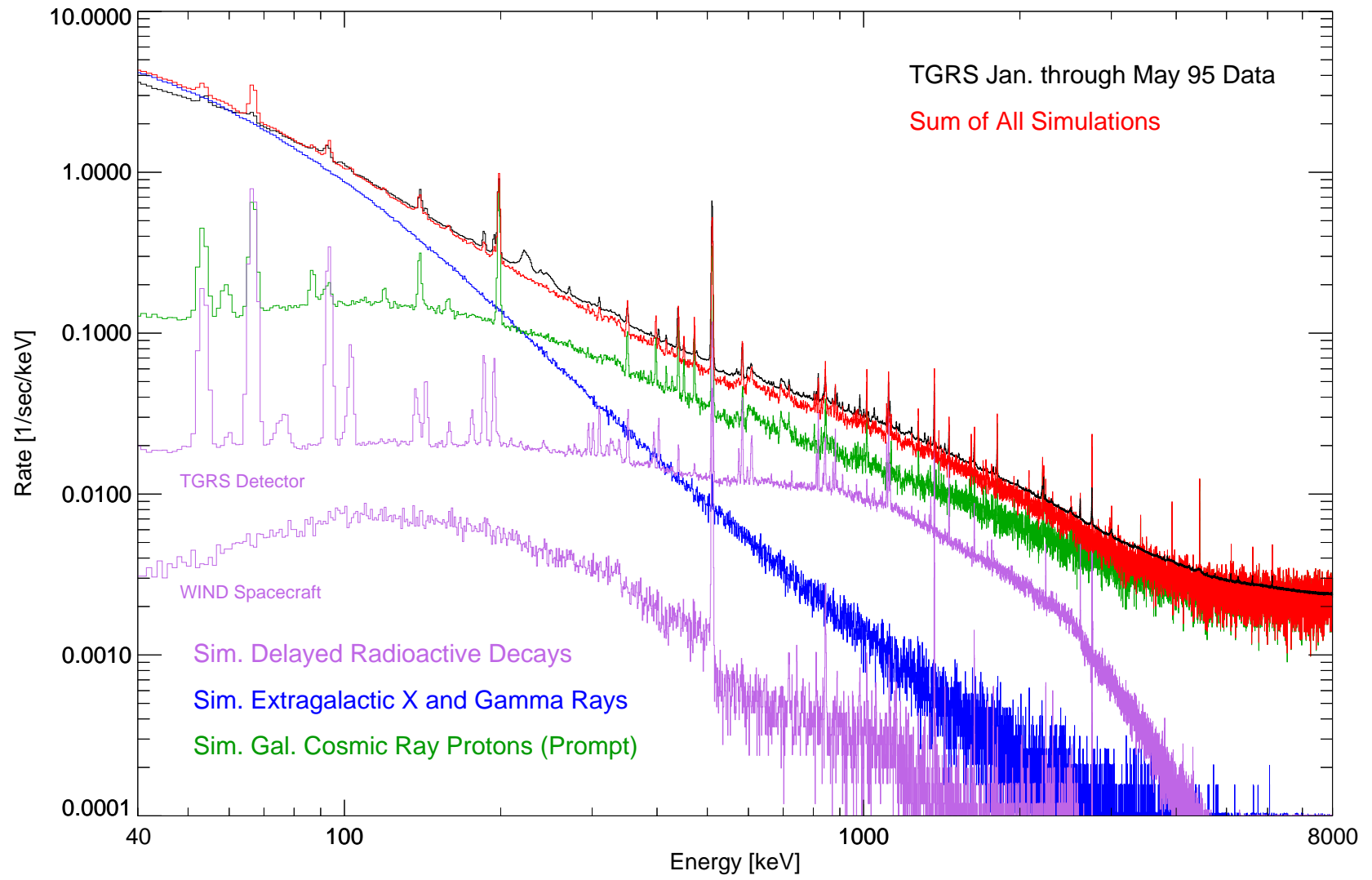


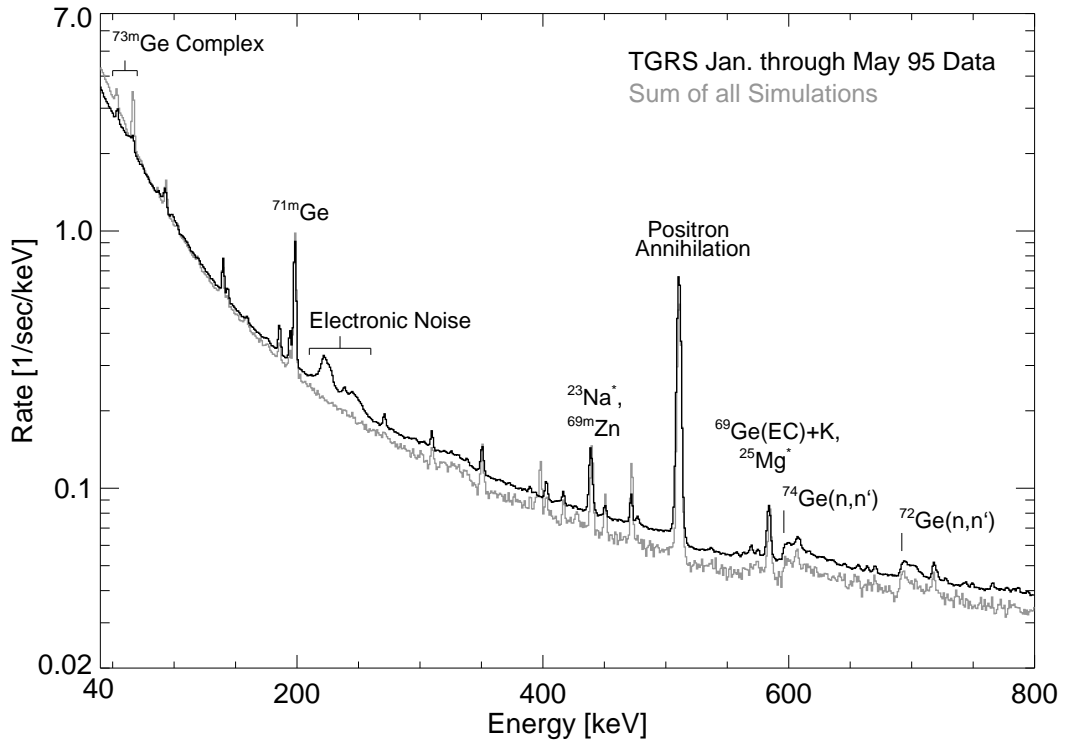


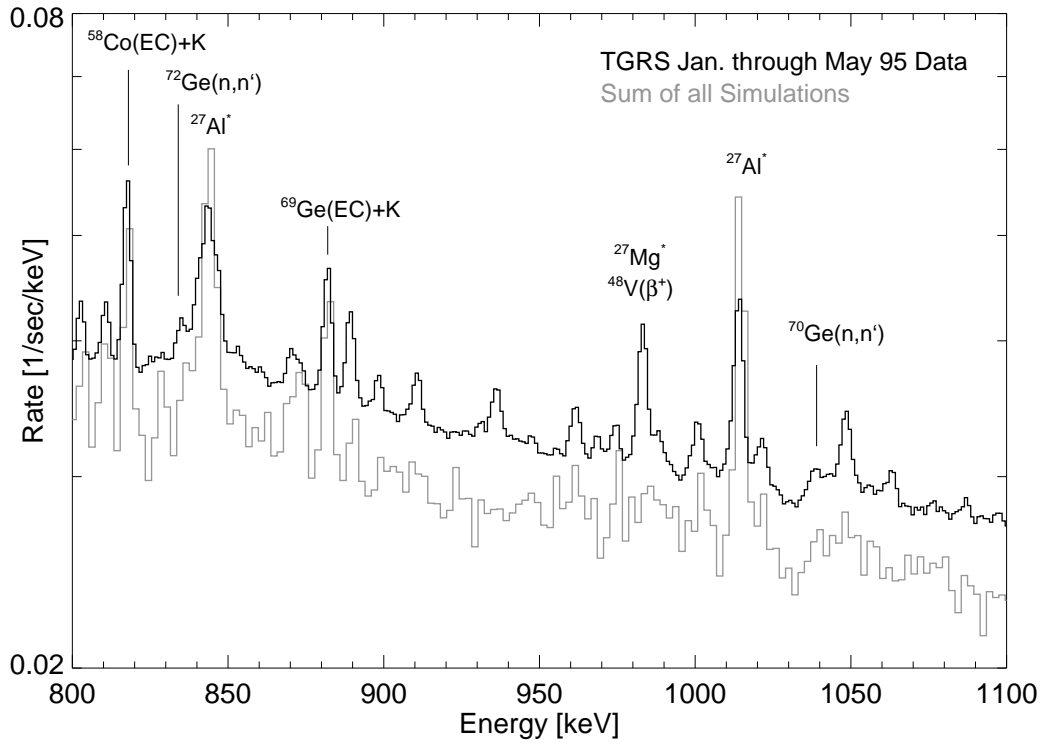


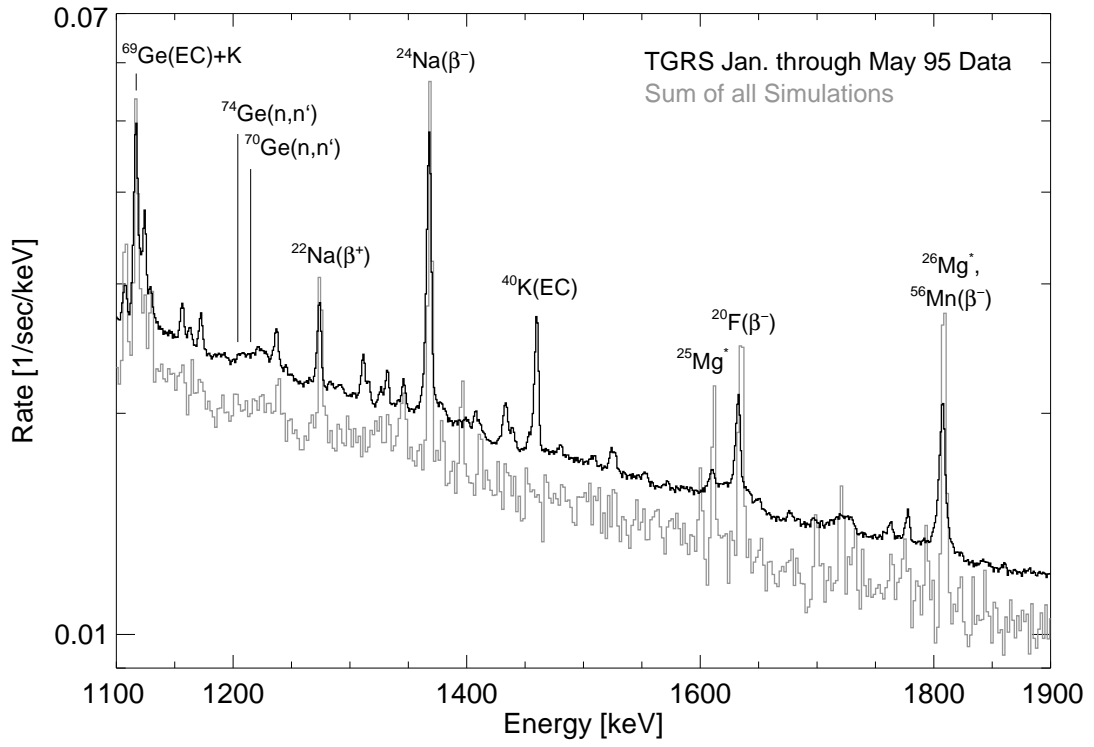
$p, n, \dots$   $\longrightarrow$

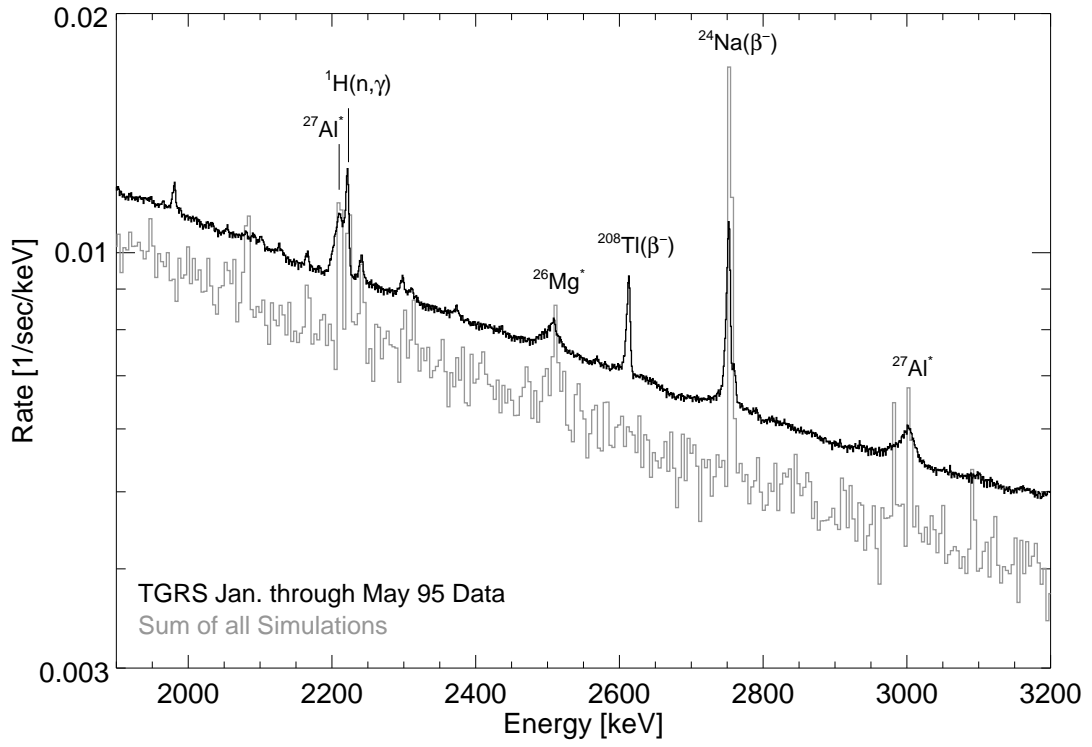


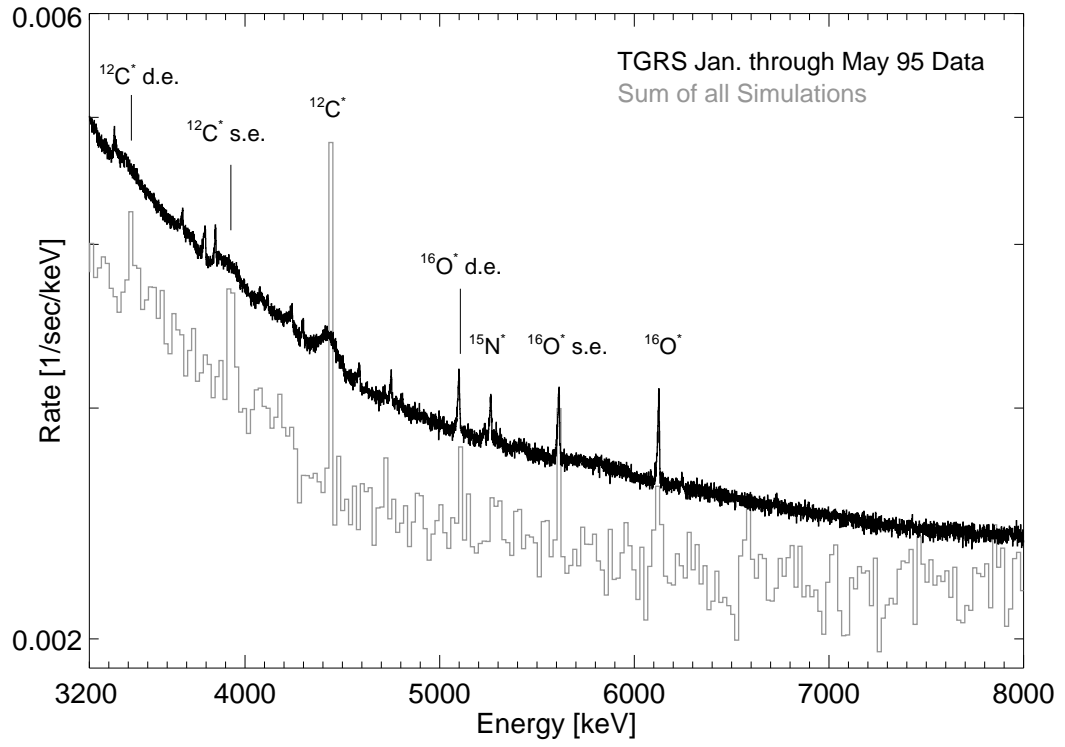


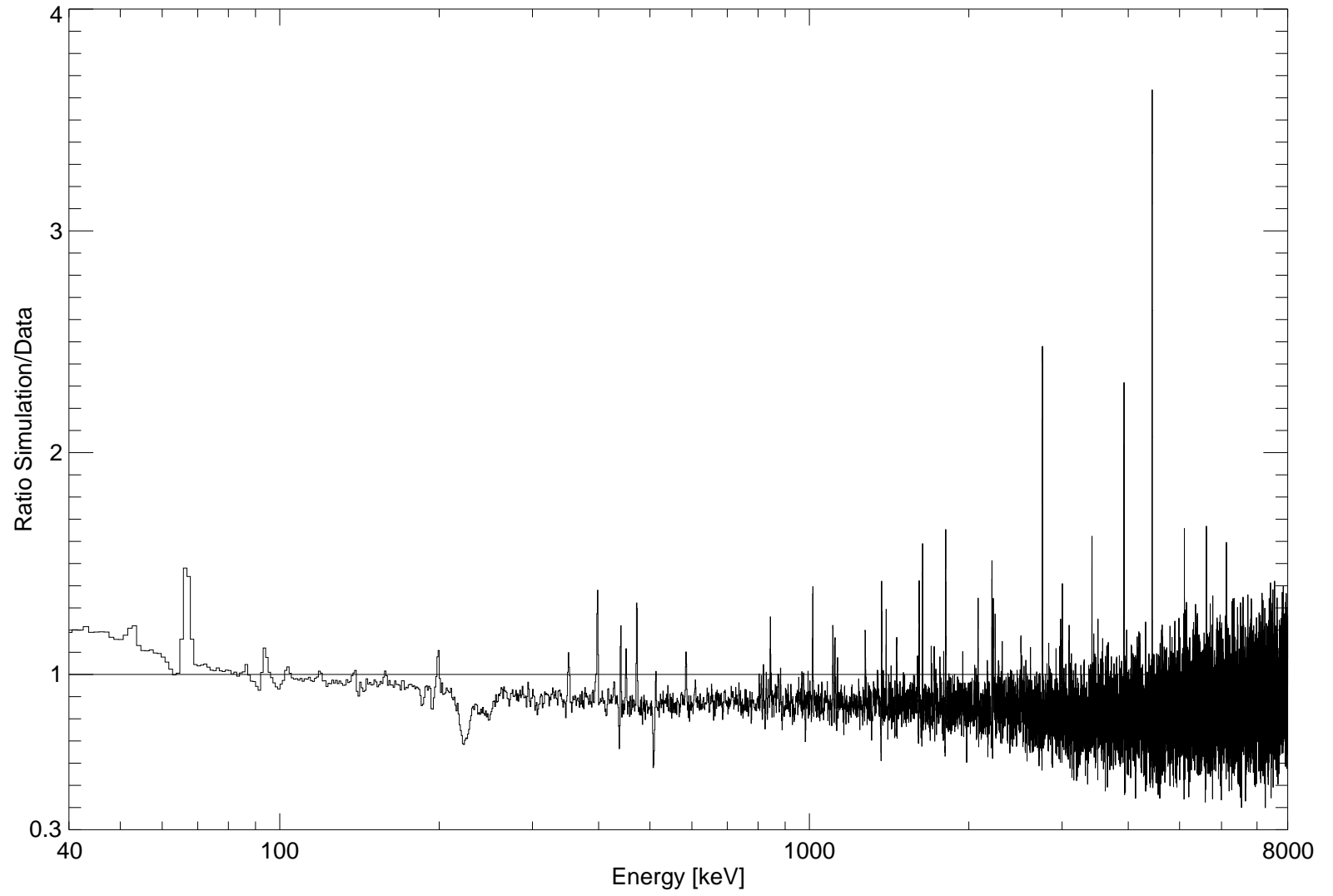


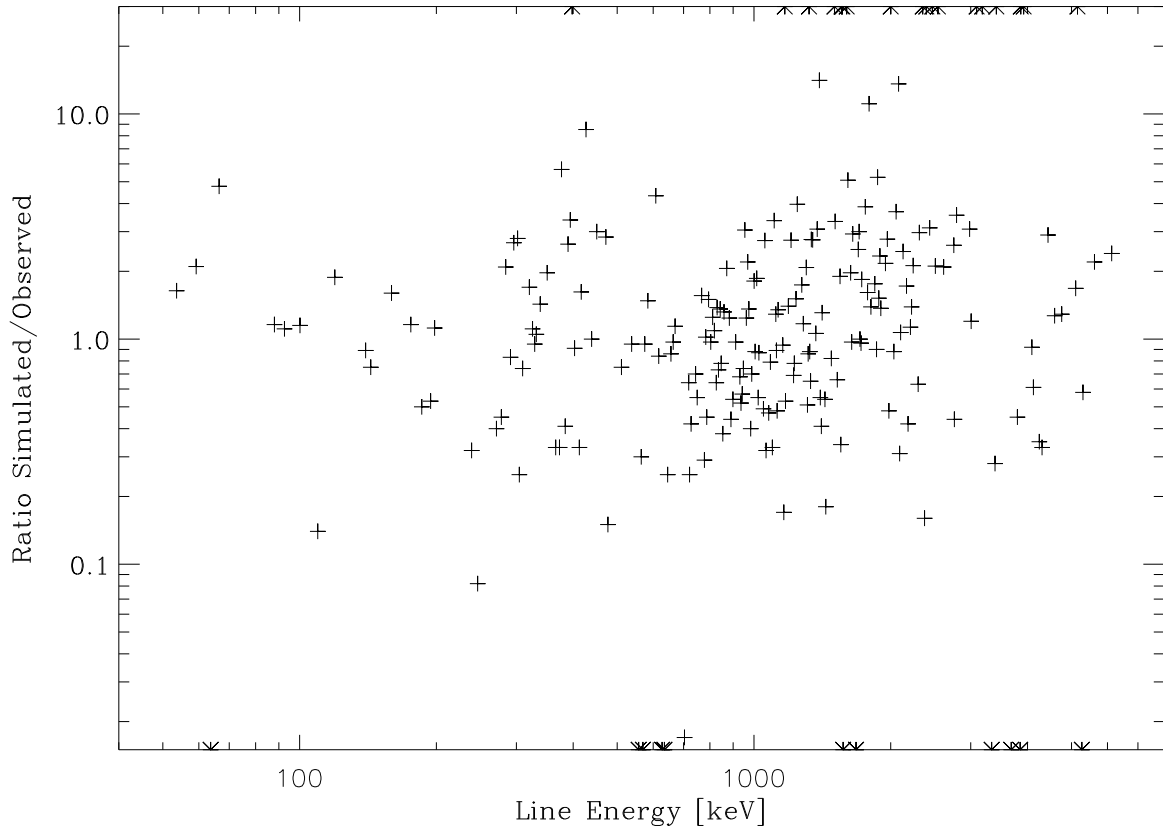












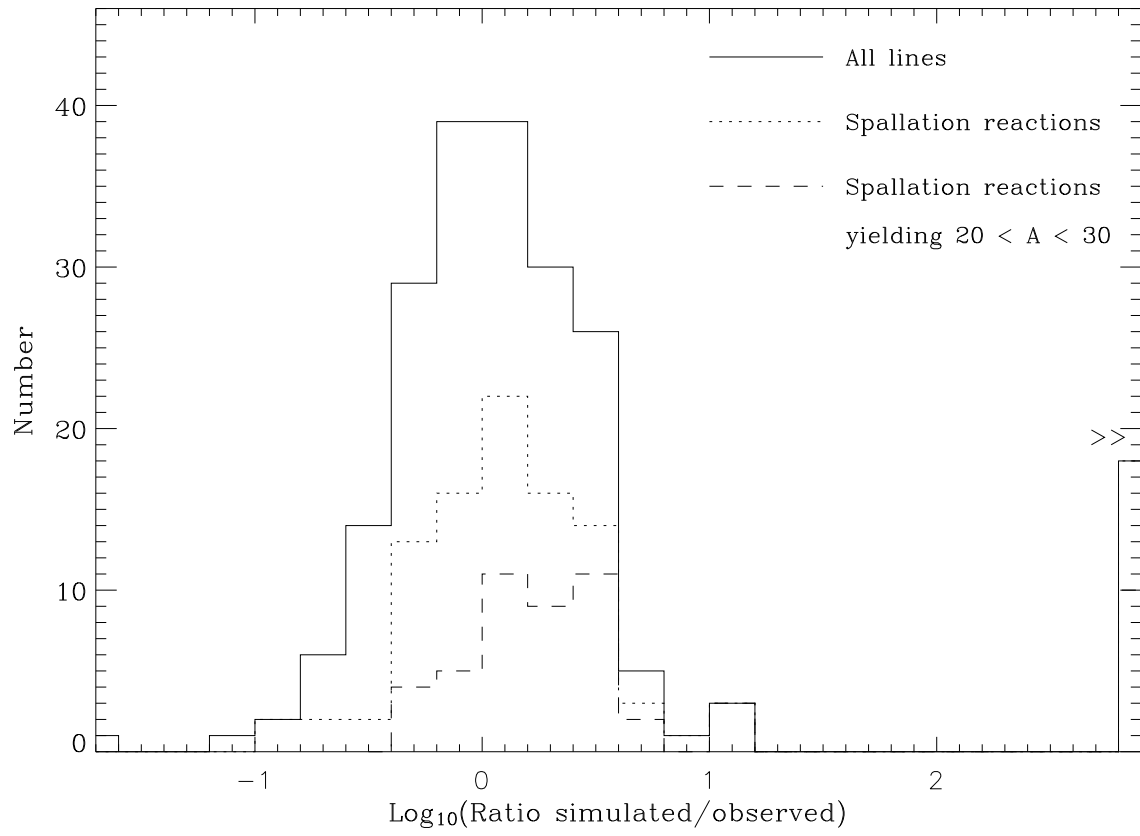


Table 1. Overview of various components of the space radiation environment discussed in more detail in the text. For each component, the main particle species are listed, together with a crude characterization of the energy spectrum, and an indication of the orbits for which they are most relevant.

Radiation Environment Component	Particle Species	Energy Spectrum <sup>a</sup> and Range <sup>b</sup>	Orbits Affected <sup>c</sup>
Galactic Cosmic Rays	p, $\alpha$	$E^{-2.7}$ , 1 GeV – 1 TeV <sup>d</sup>	All
	e	$E^{-2.6}$ , 1 – 100 GeV <sup>d</sup>	All
Solar Energetic Particles	p	$E^{-3.3}$ , $E < 200$ MeV	HEO, Balloon (LC)
Anomalous Cosmic Rays	He <sup>+</sup> , O <sup>+</sup> , Ne <sup>+</sup> , ...	10–100 MeV	HEO, Balloon (LC)
Geomagn. Trapped Rad.	p	$E^{-0.25}$ , $E < 400$ MeV	LEO
	e <sup>-</sup>	$E^{-4}$ , $E < 10$ MeV	LEO
Earth Albedo Radiation	$\gamma$	$E^{-1.7}$ , 10 keV – 1 GeV	Balloon, LEO
	n	$E^{-1.3}$ , thermal – 10 GeV	Balloon, LEO
Diffuse Cosmic Photons	$\gamma$	$E^{-2.3}$ , 50 keV – 1 GeV <sup>e</sup>	All
Intern. Prod. Background	$\gamma$	cont. & lines (10 keV–10 MeV) <sup>f</sup>	All
	n, p, e <sup>±</sup>	complex <sup>f</sup>	All

<sup>a</sup>Energy spectra are crudely approximated by power laws in order to illustrate the "hardnesses" involved. The spectra are differential intensities in units of particles per energy (and per nucleon in case of hadrons) per unit solid angle, time, and area. Energies are kinetic energy, except in the case of photons.

<sup>b</sup>The approximate range of energies covered by these spectra, as far as they are relevant for the production of instrumental background. Note that the upper bounds do not necessarily indicate where the spectrum comes to an end, but where it becomes of negligible importance. The lower bounds result from complex physical processes described in the following notes.

<sup>c</sup>Key to (idealized) orbits: Balloon — balloon altitude, near top of atmosphere; Balloon (LC) — as Balloon, but specifically at low geomagnetic cut-off (i.e. at high geographic latitudes); LEO — low-Earth orbit (will intersect radiation belts); HEO — high-Earth orbit (outside Earth's magnetosphere).

<sup>d</sup>The lower bounds and the low energy spectral shape are strongly dependent on the phase of the solar cycle (solar modulation), and for LEO even more so on orbit altitude and inclination (geomagnetic cut-off).

<sup>e</sup>At lower X-ray energies, the spectrum steepens to  $E^{-1.4}$ .

<sup>f</sup>The  $\gamma$  and particle spectra are very complex – the calculations thereof being the theme of this paper – and heavily dependent on the design of the instrument and the radiation environment in which it is operated.

Table 2. The sequence of simulation steps for Class I and Class II radiation fields. Details are explained in the text. A flow chart of MGGPOD is given in Fig. 1.

Step 1 (Class I and II)	Step 2 (Class II only)	Step 3 (Class II only)
Mass Model & Radiation Environment	Isotope Production Rates	Mass Model & Activity per Isotope and Volume
↓	↓	↓
MGEANT, GCALOR, PROMPT	ORIHET	MGEANT, GCALOR, DECAY
↓	↓	↓
Prompt Energy Deposits (Class I and II), & Isotope Prod. Rates (Class II)	Activity per Isotope and Volume	Delayed Energy Deposits

Table 3. Isotopes for which prompt de-excitation photons are generated after neutron capture and/or inelastic neutron scattering.

Process	Product Isotopes
Neutron Capture ( $n, \gamma$ )	$^{10}\text{Be}$ , $^{28}\text{Al}$ , $^{49}\text{Ti}$ , $^{53}\text{Cr}$ , $^{55,57}\text{Fe}$ , $^{64,66}\text{Cu}$ , $^{71,73,74,75,77}\text{Ge}$
Inelastic Neutron Scattering ( $n, n'\gamma$ )	$^{27}\text{Al}$ , $^{54,56,57}\text{Fe}$ , $^{63,65}\text{Cu}$ , $^{70,72,73,74,76}\text{Ge}$

Table 4. Nuclei produced by spallation for which de-excitation line probabilities were obtained from Ramaty, Kozlovsky, & Lingenfelter (1979).

Process	Product Isotopes
Spallation ( $A < 20$ )	$^{10}\text{B}$ , $^{11,12}\text{C}$ , $^{14}\text{N}$ , $^{15,16}\text{O}$ , $^{19}\text{F}$

Table 5. Identified lines; blends of identified lines.

TGRS line energy <sup>b</sup>	Count rate s <sup>-1</sup>	Transition ID (levels) <sup>b,c</sup>	Lab energy <sup>b</sup>	Comment <sup>a</sup>
53.6	0.71	<sup>73m</sup> Ge(67–13)	53.4	<i>a,s</i> ~ 15% buildup on <sup>73</sup> As τ <sub>1/2</sub> .
		<sup>65m</sup> Zn(54–g.s.)	53.9	<i>a</i> From <sup>65</sup> Ga(β <sup>+</sup> ).
		<sup>58</sup> Co(53–g.s.)	53.0	<i>s</i>
		<sup>46</sup> Sc(52–g.s.)	52.0	<i>s</i>
59.2	0.100	<sup>60m</sup> Co(59–g.s.)	58.6	<i>s</i>
		? <sup>74m</sup> Ga(60–g.s.)	59.7	<i>s</i>
66.5	0.65	<sup>73m</sup> Ge(67–13–g.s.)	66.7	<i>a,s</i> ~ 5% buildup on <sup>73</sup> As τ <sub>1/2</sub> . Two-step transition.
88.0	0.25	<sup>69m</sup> Ge(87–g.s.)	86.8	<i>a,s</i> From <sup>69</sup> As(β <sup>+</sup> )
		<sup>24</sup> Na(563–472)	91.0	<i>s</i>
92.6	0.88	<sup>67m</sup> Zn(93–g.s.)	93.3	<i>a,s</i> From <sup>67</sup> Ga(EC).
		<sup>67m</sup> Zn(93–g.s.) + L	94.5	<i>a</i> From <sup>67</sup> Ga(EC).
119.5	0.051	<sup>72m</sup> Ga(120–16–g.s.)	119.5	<i>a,s</i> Two-step transition.
139.7	0.47	<sup>75m</sup> Ge(140–g.s.)	139.7	<i>a,s</i> From <sup>75</sup> Ga(β <sup>-</sup> ).
		? <sup>57</sup> Fe(136–14–g.s.) + L	137.3	<i>a</i> From <sup>57</sup> Co(EC).
143.4	0.13	<sup>57</sup> Fe(136–14–g.s.) + K	143.6	<i>a</i> 60% buildup on <sup>57</sup> Co τ <sub>1/2</sub> .
		<sup>46m</sup> Sc(143–g.s.)	142.5	<i>s</i>
159.3	0.055	<sup>47</sup> Ti(159–g.s.)	159.4	<i>a,s</i> From <sup>47</sup> Sc(β <sup>-</sup> ).
		<sup>68</sup> As(158–g.s.)	158.1	<i>s</i>
175.7	0.031	<sup>71</sup> Ge(175–g.s.) + L	176.4	<i>a,s</i> From <sup>71</sup> As(EC).
		<sup>71</sup> Ge(175–g.s.)	174.9	<i>n</i>
185.7	0.26	<sup>67</sup> Zn(185–g.s.) + L	185.8	<i>a</i> From <sup>67</sup> Ga(EC).
		<sup>71</sup> Ge(175–g.s.) + K	186.1	<i>a</i> From <sup>71</sup> As(EC).
194.2	0.24	<sup>67</sup> Zn(185–g.s.) + K	194.2	<i>a</i> From <sup>67</sup> Ga(EC).
198.2	1.47	<sup>71m</sup> Ge(198–175–g.s.)	198.4	<i>a,s</i> From <sup>71</sup> As(β <sup>+</sup> ). Two-step transition.
		<sup>19</sup> F(197–g.s.)	197.1	<i>s,a</i> ~ 2% buildup follows solar modulation.
239.1	0.165	<sup>212</sup> Bi(239–g.s.)	238.6	<i>r</i> <sup>232</sup> Th series.
271.2	0.053	<sup>44m</sup> Sc(271–g.s.)	271.1	<i>s</i>
		<sup>228</sup> Th(328–58)	270.2	<i>r</i> <sup>232</sup> Th series.
278.0	0.026	<sup>208</sup> Pb(3475–3198)	277.4	<i>r</i> <sup>232</sup> Th series.
		<sup>228</sup> Th(1153–874)	279.0	<i>r</i> <sup>232</sup> Th series.
284.2	0.0023	<sup>61</sup> Ni(283–g.s.) + L	284.0	<i>a</i> From <sup>61</sup> Cu(EC).
291.2	0.0046	<sup>61</sup> Ni(283–g.s.) + K	291.3	<i>a</i> From <sup>61</sup> Cu(EC).
296.1	0.0153	<sup>214</sup> Bi(295–g.s.)	295.2	<i>r</i> <sup>238</sup> U series
301.8	0.0082	<sup>67</sup> Zn(394–93) + L	301.4	<i>a</i> From <sup>67</sup> Ga(EC).
304.5	0.015	<sup>75m</sup> As(304–g.s.)	303.9	<i>s</i>
309.6	0.062	<sup>67</sup> Zn(394–93) + K	309.9	<i>a</i> From <sup>67</sup> Ga(EC).
320.4	0.0056	<sup>51</sup> V(320–g.s.)	320.1	<i>a,s</i> From <sup>51</sup> Ti(β <sup>-</sup> ), <sup>51</sup> Cr(EC).
		<sup>228</sup> Th(1154–832)	321.6	<i>r</i> <sup>232</sup> Th series
325.6	0.0103	<sup>51</sup> V(320–g.s.) + K	325.6	<i>a</i> From <sup>51</sup> Cr(EC).
329.2	0.0056	<sup>228</sup> Th(328–g.s.)	328.0	<i>r</i> <sup>232</sup> Th series.
		? <sup>69</sup> Ga(319–g.s.) + K	329.0	<i>a</i> From <sup>69</sup> Ge(EC).
331.9	0.0076	<sup>21</sup> Na(332–gs)	331.9	<i>s</i>
338.5	0.013	<sup>59</sup> Ni(339–g.s)	339.4	<i>s</i>

Table 5—Continued

TGRS line energy <sup>b</sup>	Count rate s <sup>-1</sup>	Transition ID (levels) <sup>b,c</sup>	Lab energy <sup>b</sup>	Comment <sup>a</sup>
		<sup>228</sup> Th(396–58)	338.3	<i>r</i> <sup>232</sup> Th series.
350.7	0.088	<sup>21</sup> Ne(350–g.s.)	350.7	<i>s,a</i> From <sup>21</sup> Na( $\beta^+$ ).
		<sup>214</sup> Bi(352–g.s.)	351.9	<i>r</i> <sup>238</sup> U series.
373.2	0.0066	<sup>43</sup> Ca(373–g.s.)	372.8	<i>a</i> From <sup>43</sup> K( $\beta^-$ ), <sup>43</sup> Sc(EC).
377.1	0.0024	<sup>52m</sup> Mn(378–g.s.)	377.7	<i>s</i>
389.8	0.0110	<sup>25</sup> Mg(975–585)	389.7	<i>s,a</i> From <sup>25</sup> Na( $\beta^-$ ).
		<sup>214</sup> Po(1764–1378)	387.0	<i>r</i> <sup>238</sup> U series.
		<sup>214</sup> Po(2119–1730)	389.1	<i>r</i> <sup>238</sup> U series.
394.2	0.0077	<sup>67</sup> Zn(394–g.s.) + L	394.7	<i>a</i> From <sup>67</sup> Ga(EC).
402.9	0.044	<sup>67</sup> Zn(394–g.s.) + K	403.2	<i>a</i> From <sup>67</sup> Ga(EC).
416.8	0.026	<sup>26</sup> Al(417–g.s.)	416.9	<i>s</i>
426.9	0.0034	<sup>73m</sup> As(428–g.s.)	428.3	<i>s</i>
439.2	0.21	<sup>23</sup> Na(440–g.s.)	440.0	<i>s,a</i> From <sup>23</sup> Ne( $\beta^-$ ), <sup>23</sup> Mg( $\beta^+$ ).
		<sup>69m</sup> Zn(439–g.s.)	438.6	<i>s</i>
450.8	0.021	<sup>23</sup> Mg(451–g.s.)	450.7	<i>s</i>
		<sup>25</sup> Al(452–g.s.)	451.5	<i>s</i>
472.2	0.056	<sup>24m</sup> Na(472–g.s.)	472.2	<i>s</i>
477.1	0.022	<sup>7</sup> Li(478–g.s.)	477.6	<i>s</i>
511.0	2.26	<i>e</i> <sup>+</sup> annihilation	511.0	<i>s,a</i> $\sim$ 2% buildup follows solar modulation, kinematically broadened.
538.0	0.0042	<sup>59</sup> Fe(1750–1211)	537.4	<i>s</i>
564.8	0.0089	<sup>228</sup> Th(1531–969)	562.5	<i>r</i> <sup>232</sup> Th series
		<sup>54</sup> Cr(3786–3222)	563.7	<i>a</i> From <sup>54</sup> V( $\beta^-$ ).
575.1	0.021	<sup>69</sup> Ga(574–g.s.) + L	575.4	<i>a</i> From <sup>69</sup> Ge(EC).
584.0	0.125	<sup>69</sup> Ga(574–g.s.) + K	584.5	<i>a</i> From <sup>69</sup> Ge(EC).
		<sup>25</sup> Mg(585–g.s.)	585.0	<i>s</i>
		<sup>22</sup> Na(583–g.s.)	583.0	<i>s,a</i> From <sup>22</sup> Mg( $\beta^+$ ).
		<sup>208</sup> Pb(3198–2615)	583.2	<i>r</i> <sup>232</sup> Th series.
608.0	0.030	<sup>74</sup> Ge(596–g.s.) + K	606.9	<i>a</i> From <sup>74</sup> As(EC).
		<sup>214</sup> Po(609–g.s.)	609.3	<i>r</i> <sup>238</sup> U series.
656.7	0.0067	<sup>20</sup> F(656–g.s.)	656.0	<i>s</i>
		<sup>61</sup> Ni(656–g.s.) + L	657.0	<i>a</i> From <sup>61</sup> Cu(EC).
		<sup>61</sup> Ni(656–g.s.)	656.0	<i>s</i>
664.2	0.0070	<sup>61</sup> Ni(656–g.s.) + K	664.3	<i>a</i> From <sup>61</sup> Cu(EC).
		<sup>214</sup> Po(1275–609)	665.5	<i>r</i> <sup>238</sup> U series
670.4	0.0103	<sup>63</sup> Cu(670–g.s.)	669.6	<i>s</i>
		<sup>38m</sup> Cl(671–g.s.)	671.4	<i>s</i>
718.4	0.025	<sup>10</sup> B(718–g.s.)	718.3	<i>s</i>
721.4	0.0111	<sup>46</sup> Sc(774–52)	721.9	<i>s</i>
727.2	0.0101	<sup>212</sup> Po(727–g.s.)	727.3	<i>r</i> <sup>232</sup> Th series.
		<sup>228</sup> Th(1123–396)	726.9	<i>r</i> <sup>232</sup> Th series.
744.0	0.0069	<sup>52</sup> Cr(3114–2370)	744.4	<i>a</i> From <sup>52</sup> Mn(EC).
		<sup>234</sup> U(786–43)	742.8	<i>r</i> <sup>238</sup> U series.
749.9	0.0060	<sup>56</sup> Co(1720–970)	750.0	<i>a</i> From <sup>56</sup> Ni(EC).
767.0	0.0115	<sup>234</sup> U(810–43)	766.4	<i>r</i> <sup>238</sup> U series.

Table 5—Continued

TGRS line energy <sup>b</sup>	Count rate s <sup>-1</sup>	Transition ID (levels) <sup>b,c</sup>	Lab energy <sup>b</sup>	Comment <sup>a</sup>
		<sup>214</sup> Po(1378–609)	768.4	<i>r</i> <sup>238</sup> U series.
783.3	0.0041	<sup>24</sup> Na(1345–563)	781.4	<i>s</i>
		<sup>50</sup> Cr(783–g.s.)	783.3	<i>s</i>
794.5	0.0036	<sup>228</sup> Th(1123–328)	794.9	<i>r</i> <sup>232</sup> Th series.
		<sup>27</sup> Al(3004–2211)	793.0	<i>s</i>
803.4	0.0153	<sup>206</sup> Pb(803–g.s.)	803.1	<i>s</i>
811.2	0.0176	<sup>58</sup> Fe(811–g.s.) + L	811.6	<i>a</i> 50% buildup on <sup>58</sup> Co $\tau_{1/2}$ .
		<sup>58</sup> Fe(811–g.s.)	810.8	<i>a,s</i> From <sup>58</sup> Co(EC).
818.2	0.055	<sup>58</sup> Fe(811–g.s.) + K	817.9	<i>a</i> 66% buildup on <sup>58</sup> Co $\tau_{1/2}$ .
829.9	0.011	<sup>26</sup> Al(1058–228)	829.4	<i>s</i>
835.3	0.014	<sup>54</sup> Cr(835–g.s.) + L	835.5	<i>a</i> From <sup>54</sup> Mn(EC).
		<sup>54</sup> Cr(835–g.s.)	834.8	<i>a</i> From <sup>54</sup> V( $\beta^-$ ).
		<sup>228</sup> Th(1023–187)	835.7	<i>r</i> <sup>232</sup> Th series.
842.7	0.080	<sup>27</sup> Al(844–g.s.)	843.7	<i>s,a</i> From <sup>27</sup> Mg( $\beta^-$ ).
		<sup>54</sup> Cr(835–g.s.) + K	840.8	<i>a</i> From <sup>54</sup> Mn(EC).
847.0	0.036	<sup>56</sup> Fe(847–g.s.)	846.8	<i>s,a</i> 23% buildup on <sup>56</sup> Co $\tau_{1/2}$ .
854.0	0.0093	<sup>56</sup> Fe(847–g.s.) + K	853.9	<i>a</i> $\sim$ 25% buildup on <sup>56</sup> Co $\tau_{1/2}$ .
859.3	0.0068	<sup>208</sup> Pb(3475–2615)	860.6	<i>a</i> <sup>232</sup> Th series.
871.1	0.017	<sup>24</sup> Na(1341–472)	869.2	<i>s</i>
		<sup>24</sup> Na(1346–472)	874.4	<i>s</i> .
		<sup>69</sup> Ga(872–g.s.) + L	873.3	<i>a</i> From <sup>69</sup> Ge(EC).
882.7	0.038	<sup>69</sup> Ga(872–g.s.) + K	882.3	<i>a</i> From <sup>69</sup> Ge(EC).
		? <sup>21</sup> Na(3680–2798)	881	<i>s</i>
890.1	0.027	<sup>22</sup> Na(891–g.s.)	890.9	<i>s</i>
		<sup>46</sup> Ti(889–g.s.)	889.3	<i>a</i> 10% buildup on <sup>46</sup> Sc $\tau_{1/2}$ .
899.0	0.0092	<sup>204</sup> Pb(899–g.s.)	899.2	<i>s</i>
911.3	0.0138	<sup>228</sup> Th(969–58)	911.2	<i>r</i> <sup>232</sup> Th series.
		<sup>61</sup> Ni(909–g.s.)	908.6	<i>a</i> From <sup>61</sup> Co( $\beta^-$ )
931.1	0.0041	<sup>55</sup> Fe(931–g.s.)	931.3	<i>s</i>
936.5	0.0186	<sup>214</sup> Po(1543–609)	934.1	<i>r</i> <sup>232</sup> Th series.
		<sup>52</sup> Cr(2370–1434)	935.5	<i>a</i> From <sup>52</sup> Mn(EC).
		? <sup>18</sup> F(937–g.s.)	937.2	<i>s</i>
942.3	0.0046	<sup>52</sup> Cr(2370–1434) + K	941.5	<i>a</i> From <sup>52</sup> Mn(EC).
955.1	0.0020	<sup>27</sup> Mg(1940–985)	955.3	<i>s</i>
962.0	0.017	<sup>63</sup> Cu(962–g.s.)	962.1	<i>s</i>
		<sup>228</sup> Th(1023–58)	964.8	<i>r</i> <sup>232</sup> Th series.
968.8	0.0075	<sup>228</sup> Th(969–g.s.)	969.0	<i>r</i> <sup>232</sup> Th series.
974.5	0.0121	<sup>25</sup> Mg(975–g.s.)	974.4	<i>s,a</i> From <sup>25</sup> Na( $\beta^-$ ).
983.4	0.043	<sup>27</sup> Mg(985–g.s.)	984.6	<i>s</i>
		<sup>48</sup> Ti(984–g.s.)	983.5	<i>s,a</i> From <sup>48</sup> V( $\beta^+$ ).
988.9	0.0157	<sup>48</sup> Ti(984–g.s.) + K	988.5	<i>a</i> From <sup>48</sup> V(EC).
		<sup>25</sup> Mg(1965–975)	989.9	<i>s</i>
1001.2	0.0182	<sup>234</sup> U(1045–43)	1001.0	<i>r</i> <sup>238</sup> U series.
		? <sup>70</sup> Ga(1003–g.s.)	1002.6	<i>s</i>
1006.0	0.0033	<sup>26</sup> Al(3074–2070)	1004.1	<i>s</i>

Table 5—Continued

TGRS line energy <sup>b</sup>	Count rate s <sup>-1</sup>	Transition ID (levels) <sup>b,c</sup>	Lab energy <sup>b</sup>	Comment <sup>a</sup>
		<sup>53</sup> Cr(1006–g.s.)	1006.1	<i>s</i>
1014.1	0.059	<sup>27</sup> Al(1014–g.s.)	1014.4	<i>s,a</i> From <sup>27</sup> Mg( $\beta^-$ )
		<sup>26</sup> Al(2069–1058)	1011.7	<i>s</i>
1021.6	0.021	<sup>10</sup> B(1740–718)	1021.7	<i>s,a</i> From <sup>10</sup> C( $\beta^+$ ).
1025.3	0.0030	<sup>200</sup> Pb(1027–g.s.)	1026.5	<i>s,a</i> From <sup>200</sup> Bi(EC).
1049.3	0.020	<sup>66</sup> Zn(1039–g.s.) + K	1048.9	<i>a</i> From <sup>66</sup> Ga(EC).
1056.8	0.00164	<sup>20</sup> F(1057–g.s.)	1056.8	<i>a</i> From <sup>20</sup> O( $\beta^-$ ).
1063.4	0.0079	<sup>207m</sup> Pb(1064–g.s.)	1063.7	<i>s</i>
1077.9	0.0037	<sup>68</sup> Zn(1077–g.s.) + L	1078.6	<i>a</i> From <sup>68</sup> Ga(EC).
1086.8	0.0056	<sup>68</sup> Zn(1077–g.s.) + K	1087.1	<i>a</i> From <sup>68</sup> Ga(EC).
1107.9	0.0128	<sup>69</sup> Ga(1107–g.s.) + L	1108.1	<i>a</i> From <sup>69</sup> Ge(EC).
		<sup>71</sup> Ge(1096–g.s.) + K	1106.6	<i>a</i> From <sup>71</sup> As(EC).
1117.2	0.086	<sup>69</sup> Ga(1107–g.s.) + K	1117.1	<i>a</i> From <sup>69</sup> Ge(EC).
		<sup>65</sup> Cu(1116–g.s.) + L	1116.6	<i>a</i> From <sup>65</sup> Zn(EC).
		<sup>65</sup> Cu(1116–g.s.)	1115.5	<i>s</i>
1124.6	0.041	<sup>65</sup> Cu(1116–g.s.) + K	1124.5	<i>a</i> 45% buildup on <sup>65</sup> Zn $\tau_{1/2}$ .
		<sup>21</sup> Ne(2867–1746)	1121	<i>s</i>
1130.4	0.020	<sup>26</sup> Mg(2938–1809)	1129.7	<i>s</i>
1157.0	0.0128	<sup>44</sup> Ca(1157–g.s.)	1157.0	<i>a</i> From <sup>44</sup> Sc( $\beta^+$ ).
		<sup>214</sup> Po(2699–1543)	1155.6	<i>r</i> <sup>238</sup> U series.
1173.2	0.0126	<sup>60</sup> Ni(1173–g.s.)	1172.9	<i>s</i> From <sup>60</sup> Co( $\beta^-$ ).
1227.2	0.0021	<sup>42</sup> Ca(2752–1525)	1227.7	<i>a</i> From <sup>42</sup> Sc( $\beta^+$ ).
1237.5	0.011	<sup>214</sup> Po(1847–609)	1238.1	<i>r</i> <sup>238</sup> U series.
		<sup>56</sup> Fe(2085–847)	1238.3	<i>s</i>
1245.8	0.00078	<sup>56</sup> Fe(2085–847) + K	1245.5	<i>a</i> From <sup>56</sup> Co(EC).
		<sup>14</sup> C(7341–6094)	1248	<i>s</i>
1274.2	0.027	<sup>22</sup> Ne(1275–g.s.)	1274.5	<i>s,a</i> From <sup>22</sup> Na( $\beta^+$ ).
1284.1	0.0023	<sup>47</sup> Ti(1444–159)	1284.9	<i>s</i>
1303.7	0.00130	<sup>47</sup> Ti(2749–1444)	1304.6	<i>s</i>
1311.7	0.013	<sup>48</sup> Ti(2296–984)	1312.1	<i>a</i> From <sup>48</sup> V( $\beta^+$ ).
1316.4	0.0064	<sup>48</sup> Ti(2296–984) + K	1317.1	<i>a</i> From <sup>48</sup> V(EC).
1326.6	0.0049	<sup>63</sup> Cu(1327–g.s.)	1327.0	<i>s</i>
1332.3	0.0112	<sup>60</sup> Ni(1333–g.s.)	1332.5	<i>s</i> From <sup>60</sup> Co( $\beta^-$ ).
1346.5	0.0087	<sup>69</sup> Ga(1337–g.s.) + K	1347.0	<i>a</i> From <sup>69</sup> Ge(EC).
		<sup>24</sup> Na(1345–g.s.)	1344.7	<i>s</i>
		<sup>64</sup> Ni(1346–g.s.)	1345.8	<i>s</i>
1368.5	0.126	<sup>24</sup> Mg(1369–g.s.)	1368.6	<i>a,s</i> From <sup>24</sup> Na( $\beta^-$ ).
1393.4	0.00166	<sup>21</sup> Ne(1746–351)	1396	<i>s</i>
1399.7	0.0042	<sup>22</sup> Na(1984–583)	1401	<i>s</i>
1407.5	0.0070	<sup>214</sup> Po(2017–609)	1408.0	<i>r</i> <sup>238</sup> U series.
1412.8	0.0049	<sup>63</sup> Cu(1412–g.s.)	1412.1	<i>s</i>
1433.1	0.0141	<sup>52</sup> Cr(1434–g.s.)	1434.1	<i>s,a</i> From <sup>52</sup> Mn(EC).
		<sup>234</sup> U(1435–g.s.)	1435.4	<i>r</i> <sup>238</sup> U series.
		? <sup>27</sup> Al(4410–2982)	1428.1	<i>s</i>
1460.4	0.040	<sup>40</sup> Ar(1461–g.s.)	1460.8	<sup>40</sup> K calibration source.

Table 5—Continued

TGRS line energy <sup>b</sup>	Count rate s <sup>-1</sup>	Transition ID (levels) <sup>b,c</sup>	Lab energy <sup>b</sup>	Comment <sup>a</sup>
1480.4	0.0028	<sup>65</sup> Cu(1482–g.s.)	1481.8	<i>s</i>
1508.9	0.0024	<sup>24</sup> Na(1512–g.s.)	1512.3	<i>s</i>
		<sup>214</sup> Po(2119–609)	1509.2	<i>r</i> <sup>238</sup> U series.
1525.7	0.0086	<sup>22</sup> Na(1528–g.s.)	1528.1	<i>s</i>
		? <sup>42</sup> Ca(1525–g.s.)	1524.7	<i>a</i> From <sup>42</sup> Sc( $\beta^+$ ).
1546.9	0.00174	<sup>63</sup> Cu(1547–g.s.)	1547.0	<i>s</i>
1553.0	0.0025	<sup>50</sup> Ti(1554–g.s.)	1553.8	<i>a</i> From <sup>50</sup> V(EC).
1571.4	0.0016	<sup>201</sup> Pb(2507–990)	1570.8	<i>s</i>
1649.6	0.0018	<sup>26</sup> Al(2069–417)	1652	<i>s</i> 2 lines
1697.0	0.0022	<sup>27</sup> Mg(1698–g.s.)	1697.9	<i>s</i>
1721.5	0.0142	<sup>27</sup> Al(2735–1014)	1720.3	<i>s</i> Broad
1726.4	0.0075	<sup>214</sup> Po(1730–g.s.)	1729.6	<i>r</i> <sup>238</sup> U series.
		<sup>24</sup> Na double esc.	1732.0	<i>s</i>
1758.4	0.0062	<sup>214</sup> Po(1764–g.s.)	1764.5	<i>r</i> <sup>238</sup> U series.
		<sup>25</sup> Mg(2738–975)	1762.9	<i>s</i>
1778.5	0.0061	<sup>28</sup> Si(1779–g.s.)	1778.9	<i>a</i> From <sup>28</sup> Al( $\beta^-$ ).
1792.4	0.00104	<sup>25</sup> Mg(3405–1612)	1793.4	<i>s</i>
1809.0	0.049	<sup>26</sup> Mg(1809–g.s.)	1808.6	<i>s,a</i> From <sup>26</sup> Na( $\beta^-$ ).
		<sup>56</sup> Fe(2658–847)	1810.8	<i>a</i> From <sup>56</sup> Mn( $\beta^-$ ).
1844.8	0.00176	<sup>214</sup> Po(1847–g.s.)	1847.4	<i>r</i> <sup>238</sup> U series.
1861.0	0.00132	<sup>63</sup> Cu(1861–g.s.)	1861.3	<i>s</i>
1871.2	0.00031	<sup>24</sup> Na(3217–1345)	1872.0	<i>s</i>
1882.9	0.0016	<sup>15</sup> N(7155–5271)	1884.8	<i>s</i>
1902.2	0.0017	<sup>24</sup> Na(3745–1846)	1899.0	<i>s</i>
		<sup>69</sup> Ga(1892–g.s.) + K	1901.8	<i>a</i> From <sup>69</sup> Ge(EC).
1947.6	0.00115	<sup>69</sup> Ga(1924–g.s.) + K	1934.4	<i>a</i> From <sup>69</sup> Ge(EC).
1966.0	0.00115	<sup>25</sup> Mg(1965–g.s.)	1964.5	<i>s</i>
1981.6	0.0056	<sup>18</sup> O(1982–g.s.)	1982.0	<i>s</i>
2032.3	0.0015	<sup>69</sup> Ga(2024–g.s.) + K	2034.0	<i>a</i> From <sup>69</sup> Ge(EC).
2055.1	0.0012	<sup>25</sup> Mg(5462–3405)	2056.4	<i>s</i>
		<sup>23</sup> Mg(2051–g.s.)	2051	<i>s</i>
2081.3	0.0014	<sup>22</sup> Ne(3357–1275)	2082.5	<i>s,a</i> From <sup>22</sup> F( $\beta^-$ ).
2129.5	0.0022	<sup>11</sup> B(2124.7–g.s.)	2124.5	<i>s</i>
		<sup>26</sup> Mg(3941–1809)	2132.0	<i>s</i>
2166.8	0.0029	<sup>22</sup> Ne(5523–3357)	2165.9	<i>s,a</i> From <sup>22</sup> F( $\beta^-$ ).
		<sup>38</sup> Ar(2167–g.s.)	2167.4	<i>a</i> From <sup>38</sup> K( $\beta^+$ ).
2183.5	0.00085	<sup>6</sup> Li(2186–g.s.)	2186	<i>s</i>
		<sup>17</sup> O(3055–871)	2184.5	<i>a</i> From <sup>17</sup> N( $\beta^-$ ).
2209.5	0.0275	<sup>27</sup> Al(2211–g.s.)	2211.0	<i>s</i> Kinematically broadened.
		<sup>214</sup> Po(2204–g.s.)	2204.2	<i>r</i> <sup>238</sup> U series.
2220.3	0.0171	<i>p(n,<math>\gamma</math>)d</i> direct capture	2223	<i>n</i>
2241.3	0.0051	<sup>24</sup> Mg single esc.	2243.0	<i>a</i> From <sup>24</sup> Na( $\beta^-$ ).
2312.0	0.0030	<sup>14</sup> N(2313–g.s.)	2312.6	<i>s</i>
2436.4	0.00077	<sup>21</sup> Ne(2789–351)	2438	<i>s</i>
2508.0	0.0109	<sup>26</sup> Mg(4318–1809)	2509.6	<i>s</i> Broad (kinematics?).

Table 5—Continued

TGRS line energy <sup>b</sup>	Count rate s <sup>-1</sup>	Transition ID (levels) <sup>b,c</sup>	Lab energy <sup>b</sup>	Comment <sup>a</sup>
2614.9	0.0139	<sup>208</sup> Pb(2614.6–g.s.)	2614.5	<i>r</i> <sup>232</sup> Th series.
		<sup>20</sup> Ne(4248–1634)	2613.8	<i>s</i>
2753.7	0.028	<sup>24</sup> Mg(4123–1369)	2754.0	<i>a,s</i> From <sup>24</sup> Na( $\beta^-$ ).
2761.4	0.0045	<sup>66</sup> Zn(2752–g.s.) + K	2761.6	<i>a</i> From <sup>66</sup> Ga(EC).
2981.8	0.0038	<sup>27</sup> Al(2982–g.s.)	2981.8	<i>s</i> Broad.
		<sup>23</sup> Na(2982–g.s.)	2981.9	<i>s</i>
3003.1	0.0120	<sup>27</sup> Al(3004–g.s.)	3004.0	<i>s</i> Broad (kinematics?).
3336.0	0.00175	<sup>13</sup> C single esc.	3342.2	<i>s</i>
3404	0.009	<sup>12</sup> C double esc.	3416.0	<i>s</i> Kinematically broadened.
3683.9	0.0015	<sup>13</sup> C(3684–g.s.)	3683.9	<i>s</i>
3800.4	0.0029	<sup>66</sup> Zn(3792–g.s.) + K	3801.2	<i>a</i> From <sup>66</sup> Ga(EC).
3853.5	0.00171	<sup>13</sup> C(3854–g.s.)	3853.2	<i>s</i>
		? <sup>24</sup> Mg(5235–1369)	3866.2	<i>s</i>
3920	0.012	<sup>12</sup> C single esc.	3927.0	<i>s</i> Kinematically broadened.
4090.0	0.0017	<sup>66</sup> Zn(4086)–g.s.) + K	4095.9	<i>a</i> From <sup>66</sup> Ga(EC).
4122.3	0.00094	<sup>24</sup> Mg(4122.6–g.s.)	4122.7	<i>s,a</i> Sum peak. From <sup>24</sup> Na( $\beta^-$ ).
4246.8	0.0017	<sup>15</sup> N double esc.	4247.2	<i>s</i>
4306.3	0.0013	<sup>66</sup> Zn(4296–g.s.) + K	4305.5	<i>a</i> Both from <sup>66</sup> Ga(EC).
		<sup>66</sup> Zn(4296–g.s.) + L	4297.1	<i>a</i>
4431	0.015	<sup>12</sup> C(4439–g.s.)	4438.0	<i>s</i> Kinematically broadened.
4588.9	0.0015	<sup>14</sup> N single esc.	4593.8	<i>s</i>
4757.3	0.0017	<sup>15</sup> N single esc.	4758.2	<i>s</i>
5106.0	0.0037	<sup>16</sup> O double esc.	5106.6	<i>s</i>
		<sup>14</sup> N(5106–g.s.)	5104.9	<i>s</i>
5269.3	0.0026	<sup>15</sup> N(5270–g.s.)	5269.2	<i>s</i>
5289.	0.0021	<sup>15</sup> N(5298–g.s.)	5297.8	<i>s</i> Broad ???
5298.0	0.00048	<sup>15</sup> N(5298–g.s.)	5297.8	<i>a</i> From <sup>15</sup> C( $\beta^-$ )
5420.	0.0013	?	?	? Broad
5617.8	0.0044	<sup>16</sup> O single esc.	5617.6	<i>s</i>
6128.7	0.0052	<sup>16</sup> O(6129–g.s.)	6128.6	<i>s</i>
6242.1	0.00006	?	?	?
6723.6	0.00005	?	?	?

<sup>a</sup>Key to reaction types: *a* —  $\beta$ -decay after activation; *s* — spallation followed by prompt de-excitation; *n* — (*n*, $\gamma$ ) or (*n*,*n'*) followed by prompt de-excitation; *r* — natural radioactivity.

<sup>b</sup>All energies in keV.

<sup>c</sup>K and L are atomic sub-shell binding energies in cases of electron capture (EC).

Table 6. Blends containing unidentified lines.

TGRS line energy, keV	Count rate s <sup>-1</sup>	Transition ID (levels, keV) <sup>b</sup>	Nominal energy, keV		Comment <sup>a</sup>
63.7	0.35	? <sup>65m</sup> Ni(63-g.s.)	63.4	<i>s</i>	
75.6	0.24	? <sup>61</sup> Ni(67-g.s.) + K	75.3	<i>a</i>	From <sup>61</sup> Cu(EC).
		? <sup>66</sup> Ga(66-g.s.) + K	75.5	<i>a</i>	From <sup>66</sup> Ge(EC).
100.2	0.45	<sup>67</sup> Zn(93-g.s.) + K	103.0	<i>a</i>	From <sup>67</sup> Ga(EC).
109.6	0.22	<sup>19</sup> F(110-g.s.)	109.9	<i>s</i>	
246.5	0.225	<sup>214</sup> Bi(295–53)	242.0	<i>r</i>	<sup>238</sup> U series.
		<sup>69</sup> Ga(1107–872) + K	245.2	<i>a</i>	From <sup>69</sup> Ge(EC).
264.9	0.0031	? <sup>75</sup> As(265-g.s.)	264.7	<i>s</i>	Weak
366.1	0.0055	? <sup>73</sup> Ge(364–67–13-g.s.)	364.3	<i>n</i>	Three-step transition.
		? <sup>200</sup> Hg(368-g.s.)	367.9	<i>a</i>	From <sup>200</sup> Tl(EC).
384.3	0.0088	<sup>62</sup> Cu(426–41)	385.3	<i>s</i>	
412.8	0.0082	<sup>228</sup> Th(1432–1023)	409.5	<i>r</i>	<sup>232</sup> Th series.
		<sup>54</sup> Fe(2949–2538)	411.4	<i>a</i>	From <sup>54</sup> Co( $\beta^+$ ).
		? <sup>198</sup> Hg(412-g.s.)	411.8	<i>a</i>	From <sup>198</sup> Tl(EC).
557.4	0.0056	? <sup>62</sup> Cu(548-g.s.) + K	557.3	<i>a</i>	From <sup>62</sup> Zn(EC).
569.5	0.0183	<sup>207</sup> Pb(570-g.s.)	569.6	<i>s</i>	
617.2	0.0031	<sup>43</sup> Ca(990–373)	617.5	<i>a</i>	From <sup>43</sup> K( $\beta^-$ ).
627.9	0.0043	<sup>63</sup> Zn(627-g.s.) + L	628.3	<i>a</i>	From <sup>63</sup> Ga(EC).
		? <sup>201m</sup> Pb(629-g.s.)	629.1	<i>a</i>	From <sup>201</sup> Bi(EC).
635.2	0.0056	<sup>63</sup> Zn(637-g.s.) + L	638.2	<i>a</i>	From <sup>63</sup> Ga(EC).
		<sup>63</sup> Zn(627-g.s.) + K	636.8	<i>a</i>	From <sup>63</sup> Ga(EC).
		? <sup>71</sup> Ge(831–525–198)	633.1	<i>n</i>	Two-step transition.
645.8	0.0032	<sup>63</sup> Zn(637-g.s.) + K	646.0	<i>a</i>	From <sup>63</sup> Ga(EC).
703.2	0.082	? <sup>53m</sup> Fe(3040–2339)	701.1	<i>a</i>	From <sup>53</sup> Co( $\beta^+$ ).
		<sup>234</sup> U(1554–852)	701.6	<i>r</i>	<sup>238</sup> U series.
777.9	0.0056	<sup>228</sup> Th(1168–396)	772.3	<i>r</i>	<sup>232</sup> Th series.
787.2	0.0073	? <sup>201</sup> Pb(1415–629)	786.4	<i>a</i>	From <sup>201</sup> Bi(EC).
		<sup>234</sup> U(786-g.s.)	786.3	<i>r</i>	<sup>238</sup> U series.
826.2	0.0036	? <sup>60</sup> Ni(2159–1333)	826.1	<i>a</i>	From <sup>60</sup> Cu( $\beta^+$ ).
		<sup>20</sup> F(823-gs)	822.7	<i>s</i>	
851.1	0.0077	?		<i>s</i>	Energy from simulation.
947.8	0.0054	? <sup>40</sup> Ar single esc.	949.8		From <sup>40</sup> K calibration source.
1005.9	0.0033	<sup>26</sup> Al(3074–2069)	1004.1	<i>s</i>	
		? <sup>48</sup> V(2062–1056)	1006.3	<i>s</i>	
1097.7	0.0044	<sup>228</sup> Th(1153–58)	1095.7	<i>r</i>	<sup>232</sup> Th series.
		<sup>208</sup> Pb(3708–2615)	1093.9	<i>r</i>	<sup>232</sup> Th series.
1120.6	0.020	<sup>46</sup> Ti(2010–889)	1120.5	<i>a</i>	From <sup>46</sup> Sc(EC).
		<sup>21</sup> Ne(2867–1746)	1121	<i>s</i>	
1163.5	0.0070	<sup>44</sup> Ca(1157-g.s.) + K	1161.1	<i>a</i>	From <sup>44</sup> Sc(EC).
		<sup>62</sup> Ni(2336–1173)	1163.4	<i>s</i>	
1190.7	0.0040	<sup>61</sup> Ni(1185-g.s.) + K	1193.6	<i>a</i>	From <sup>61</sup> Cu(EC).
		<sup>234</sup> U(1237–43)	1193.8	<i>r</i>	<sup>238</sup> U series.
1206.9	0.00131	? <sup>200</sup> Hg(1574–368)	1205.7	<i>a</i>	From <sup>200</sup> Tl(EC).
1222.2	0.0029	? <sup>24</sup> Na(2563–1345)	1218.1	<i>s</i>	
1337.6	0.0013	<sup>69</sup> Ga(1337-g.s.) + L	1338.0	<i>a</i>	From <sup>69</sup> Ge(EC).

Table 6—Continued

TGRS line energy, keV	Count rate $s^{-1}$	Transition ID (levels, keV) <sup>b</sup>	Nominal energy, keV	Comment <sup>a</sup>
1378.0	0.0051	<sup>214</sup> Po(1378–g.s.)	1377.7	<i>r</i> <sup>238</sup> U series.
		<sup>57</sup> Co(1378–g.s.)	1377.6	<i>a</i> From <sup>57</sup> Ni(EC).
1439.2	0.0064	<sup>52</sup> Cr(1434–g.s.) + K	1440.1	<i>a</i> From <sup>52</sup> Mn(EC).
1609.6	0.0063	<sup>25</sup> Mg(1612–g.s.)	1611.7	<i>s,a</i> From <sup>25</sup> Na( $\beta^-$ ).
1632.1	0.032	<sup>20</sup> Ne(1634–g.s.)	1633.6	<i>a,s</i> From <sup>20</sup> F( $\beta^-$ ).
		<sup>23</sup> Na(2076–440)	1636.0	<i>s</i>
1641.2	0.0015	? <sup>38</sup> Ar(3810–2167)	1642.7	<i>s</i>
1677.9	0.0053	<sup>58</sup> Fe(1675–g.s.) + K	1681.8	<i>a</i> From <sup>58</sup> Co(EC).
1703.9	0.0012	? 2211–2223 keV line	~ 1700	<i>s</i>
		complex single escape		
1711.4	0.0024	? <sup>73</sup> As(1796–84)	1712.1	<i>s</i>
1893.3	0.0014	? <sup>63</sup> Cu(2858–962)	1895.6	<i>s</i>
		? <sup>203</sup> Pb(2713–820)	1893.0	<i>a</i> From <sup>203</sup> Bi(EC).
2092.2	0.0014	?	2092.5	<i>a</i> Line energy from simulation.
2103.0	0.00164	? 2614 keV single esc.	2103.5	<i>r,s</i>
2298.4	0.0038	<sup>15</sup> N(7566–5271)	2296.8	<i>s</i>
		<sup>11</sup> B(6743–4445)	2297.8	<i>s</i>
		?	2300.5	<i>a</i> Line energy from simulation.
2373.8	0.00184	<sup>64</sup> Zn(2374–g.s.) + L	2375.5	<i>a</i> From <sup>64</sup> Ga( $\beta^+$ ).
2792.2	0.00076	? <sup>21</sup> Ne(2794–g.s.)	2794	<i>s</i> Weak.
3393.3	0.00058	<sup>66</sup> Zn(3381–g.s.) + K	3391.0	<i>a</i> From <sup>66</sup> Ga(EC).

<sup>a</sup>Key to reaction types: *a* —  $\beta$ -decay after activation; *s* — spallation followed by prompt de-excitation; *n* — (*n*, $\gamma$ ) or (*n*,*n'*) followed by prompt de-excitation; *r* — natural radioactivity.

<sup>b</sup>K and L are atomic sub-shell binding energies in cases of electron capture (EC).

Table 7. A comparison of the simulated and the observed count rate in triangular or “sawtooth” shaped features that arise from inelastic neutron scattering in the Ge detector (see Figs. 6 and 7). For the two limiting cases of a low and a high estimate of the underlying continuum, refer to text.

Underlying state, keV	Energy range, keV	Low Cont. Estimate		High Cont. Estimate	
		Sim., $s^{-1}$	Obs., $s^{-1}$	Sim., $s^{-1}$	Obs., $s^{-1}$
596 ( <sup>74</sup> Ge)	592–686	0.66	0.6	0.37	0.28
692 ( <sup>72</sup> Ge)	687–760	0.30	0.35	0.09	0.06
834 ( <sup>72</sup> Ge)	831–866	0.105	0.053	0.074	0.013
1039 ( <sup>70</sup> Ge)	1031–1083	0.166	0.094	0.087	0.070
1204 ( <sup>74</sup> Ge), 1215 ( <sup>70</sup> Ge)	1200–1260	0.153	0.109	0.070	0.061